Cu-BTC functional microdevices as smart tools for capture and preconcentration of nerve agents

F. Almazán, [1] M.A. Urbiztondo,[1, 2] P. Serra-Crespo,[3] B. Seoane,[4] J. Gascon,[4, 5] J. Santamaría,[1, 6, 7] M.P. Pina[1, 6, 7]

[1] Nanoscience Institute of Aragon (INA), Univ. Zaragoza, Department of Chemical & Environmental Engineering, Campus Rio Ebro, C/Mariano Esquillor s/n, 50018 Zaragoza, Spain

[2] Centro Universitario de la Defensa de Zaragoza, Carretera Huesca s/n, 50090 Zaragoza, Spain

[3] Applied Radiation and Isotopes, Department of Radiation Science and Technology, Faculty of Applied Sciences, Technical University Delft, Mekelweg 15, 2629 JB, Delft, the Netherlands

[4] Catalysis Engineering, Department of Chemical Engineering, Delft University of Technology, Van der Maasweg 9, 2629 HZ Delft, The Netherlands

[5] Advanced Catalytic Materials, KAUST Catalysis Center, King Abdullah University of Science and Technology, Thuwal 23955, Saudi Arabia

[6] Networking Research Center on Bioengineering, Biomaterials and Nanomedicine, CIBER-BBN, 28029 Madrid, Spain

[7] Univ Zaragoza, CSIC, Instituto de Ciencia de Materiales de Aragón (ICMA), C/Pedro Cerbuna 12, 50009 Zaragoza, Spain

ABSTRACT: Cu-based Metal Organic Frameworks (MOF) microdevices are applied in sampling and preconcentration of nerve agents (NAs) diluted in gaseous streams. An *in-situ* electrochemical assisted synthesis of Cu-BTC thick film is carried out to functionalize a Cu modified glass substrate. This simple, rapid, reproducible and easy to integrate MOF synthesis approach, enables the microfabrication of functional microprenconcentrators with large BET surface area (above 2000 cm^2) and active pore volume (above 90 nanoliters) for the efficient adsorption of nerve agent molecules along the microfluidic channel 2.5 cm in length. Equilibrium adsorption capacity of the bulk material has been characterized through thermogravimetric analysis after exposure to controlled atmospheres of a sarin gas surrogate, dimethyl methylphosphonate (DMMP), in both dry and humid conditions (30% RH at 293 K). Breakthrough tests at ppm level (162 mg/m^3) reveal equilibrium adsorption capacities up to 691 mg/g. The preconcentration performance of such μ-devices when dealing with highly diluted surrogate atmosphere, i.e. 520 ppbV (2.6 mg/m^3) at 298 K, leads to preconcentration coefficients up to 171 for sample volume up to 600 STP cm^3. We demonstrate the potentialities of Cu-BTC micropreconcentrators as smart first responder tools for "on field" detection of nerve agents in gas phase at relevant conditions.

INTRODUCTION

Vulnerability of critical indoor infrastructures to intentional nerve agents release poses a significant point of concern for authorities responsible for incident preparedness and prevention. Such chemical compounds are odorless, colorless, highly persistent, volatile and lethal even at low concentration.[1] Particularly, the organophosphonates-based nerve agents (NAs), where the well-known sarin and soman gases belong to, have been used against civilian population in shocking terrorist attacks. Infamously known are the terrorist attack in the subway of Tokyo in 1991 and the recent ones against civilians in Syria.[2] A few studies are available for sarin vapor exposures on human volunteers in order to directly derive acute exposure guideline levels. Results indicate that the threshold for miosis and other minimal toxic effects falls in the range of $0.05 - 0.5$ mg/m^3 ($9 - 87$ ppbV) for 30 - 10 min exposures, respectively.[3]

Due to the potential threat that NAs constitute against the population, many efforts have been dedicated to its early detection. To improve the limit of detection of the available equipment, a common solution is to implement a trapping-preconcentration unit upstream the detector. This approach has been successfully applied in many fields where the identification of compounds at very low concentration (sub ppmV) is required; such as workplace health and safety[4] or for non-invasive, diagnostic tools based on the detection of exhaled volatile biomarkers[5]. Enrichment factors up to 300 have been reported for aromatic VOCs using carbon nanotubes-based µ-preconcentrators for 100 ppbV feed concentration and sample volume up to 400 STP cm^3.[6]

MOFs are hybrid materials composed of coordinatively linked metal ions or clusters via organic ligands to form porous crystalline frameworks with proven microporosity. Compared to microporous zeolites or mesoporous silica, MOFs exhibit higher chemical versatility. Remarkable adsorption capacities have been reported towards organophosphonate compounds.

61 The isoreticular IRMOF-1 $Zn_4O(dmcapz)_3$, dmcapz stands for 4-carboxy-3,5-

62 dimethylpyrazolate, exhibits an adsorption capacity up to 950 mg DMMP/g IRMOF-1 for

63 saturated atmosphere of dimethyl methylphosphonate (DMMP) at 50 ºC [7]; as well as mild

64 adsorption heat values (-ΔH_{ads} = 44.8 kJ/mol for diisopropylfluorophosphate (DIFP) at

65 temperatures ranging from 383 to 513 K [8]). Newly developed Zr-based MOFs, such as NU-1000,

66 UiO-66 or MOF-808, have attracted interest in NAs decontamination not only due to their

67 sorption properties (713 mgDMMP/gNU-1000 and 152 mgDMMP/gUiO-66 for 507 mg/m^3

68 DMMP at 298K [9]) but also due to their catalytic properties towards organophosphorus

69 degradation by hydrolysis.[10]

70 Cu-based MOFs, such as Cu-BTC (HKUST-1), have also been widely reported as adequate

71 adsorbents for organophosphorous vapors due the high affinity that those compounds exhibit

72 towards Cu clusters and the stability of the resulting metal complexes. Fourier-transformation

73 infrared (FTIR) spectroscopy analysis on surface acoustic wave type sensors functionalized via

74 self-assembled monolayer with –$(CO_2)_2Cu$ as terminal group and exposed to diisopropyl

75 methylphosphonate (DIMP) in gas phase reveal the formation of Cu–DIMP complexes (P=O-

76 Cu). [11] The affinity of organophosphorous compounds to copper ions still prevails in HKUST-1

77 as demonstrated by the experimentally measured adsorption heat value for

78 diisopropylfluorophosphate (DIFP), -ΔH_{ads} = 48.4 kJ/mol, which is higher than that observed for

79 commercial Carboxen, -ΔH_{ads} = 38.3 kJ/mol.[12] Finally, theoretical computational models[13] using

80 density functional theory (DFT) point out that the most favorable MOFs, among the 1544 MOFs

81 tested, for Sarin gas adsorption are those with pore sizes in the range of 6-8 Å. Smaller pores

82 cannot accommodate Sarin molecules and on larger pores the molecular interactions with the

83 framework become weaker. Accordingly, Cu-BTC emerges as potential adsorbent for

84   organophosphonates compounds thanks to its pore size distribution[14] and the chemical affinity of

85   the Cu nodes. Thus, well-intergrowth layers of Cu-BTC on microfluidic devices are herein

86   explored to capture and preconcentrate DMMP, a Sarin surrogate, from highly diluted gas

87   streams.

88   The synthesis of MOF films has been particularly of interest in the field of chemical sensors[15]

89   and gas membranes for selective separations[16]. Novel approaches such as microfluidic pen

90   lithography[17] or inkjet printing technology are gaining importance due to their potential for large

91   scale manufacturing of functional microdevices. Recently, UiO-66 has been synthesized in situ

92   by inkjet printing on resonant Si microcantilevers with piezoresistive detection, which have been

93   applied to DMMP sensing with theoretical limit of detection down to 0.025 mg/m^3 (5 ppbV).[18]

94   In this work, in situ electrochemical growth of Cu-BTC, a well-known MOF material that has

95   been extensively investigated both experimentally and theoretically, on a glass modified

96   substrate is carried out to functionalize μ-preconcentrators for NAs[19,20] in order to demonstrate

97   the potentialities for capture and preconcentration applications. The micropatterned Cu electrode

98   is exposed to the electrolyte solution and used as metal source for the in situ electrochemical

99   synthesis of Cu-BTC films following a similar approach to our previous publications[21]. The work

100   is divided in two parts. The first part is devoted to study the influence of the current density and

101   number of electrosynthesis cycles on the heterogeneous MOF crystallization rate, crystal

102   morphology and surface coverage of the glass substrate. Special attention is paid to the nature of

103   the Cu adhesion promoters (Au-Cr vs. Ti). As a result, an optimum potentiometric procedure is

104   defined for the fabrication of functional microdevices based on Cu-BTC films. The second part

105   is focused on the adsorption performance of the functional μ-preconcentrators towards DMMP.

106   Equilibrium uptake values, dynamic adsorption properties from breakthrough tests at ppmV level

107   and preconcentration coefficients are evaluated and compared with published data. Furthermore,

108   the molecular interactions of DMMP with Cu-BTC and Cu/Cu_2O surfaces in dry and humid

109   conditions are computationally studied to gain insight into the experimental results. Thus, this

110   work constitutes one of the still very scarce reports on MOF based functional microdevices. To

111   the best of our knowledge, continuous Cu-BTC films and Si based microfluidic devices are

112   combined for the first time to be employed efficiently in sampling and preconcentration

113   applications of toxic compounds.

114   **EXPERIMENTAL SECTION**

115   **µ-preconcentrator fabrication**

116   The µ-preconcentrator device is composed of two parts: 1) a microfluidic channel on a Si

117   substrate and 2) a glass substrate where the adsorbent is synthesized. The microfluidic channel,

118   2.5cm length and 20 µm depth, on un-doped <100>-oriented, polycrystalline 500 ± 20 µm Si

119   wafer is fabricated as previously described.[22] Channel depth has been confirmed by profilometry.

120   Each 4-inch Si wafer contains 8 different microdevices substrates, which are diced apart after the

121   process is finished (see Section 1 of the Supporting Information).

122   The electrochemical synthesis of the Cu-BTC was performed on the micropatterned copper on

123   the Borofloat substrate as electrodes (Sigert Wafer, 500 ± 20 µm thickness, surface roughness <

124   1.2 nm). In particular, two different Cu modified glass substrates have been investigated (Figure

125   1) to analyze the influence of the metal adhesion layer: i) 200 nm of Cu over an adhesion layer of

126   10 nm Cr and 50 nm Au denoted as Cu-Cr/Au substrate (0.52 cm^2 metallized surface) and ii) 500

127   nm Cu over an adhesion layer of 40 nm Ti denoted as Cu-Ti substrate (0.69 cm^2 metallized

128   surface). The finished Borofloat wafer is also diced in 8 different substrates and processed

129   individually.

130   After the Cu-BTC MOF synthesis, the Borofloat substrate is bonded to its Si counterpart by

131   anodic bonding and fluidic ports were inserted to connect to transfer lines. Computer modelling

132   in COMSOL Multiphysics of the microfluidic device was performed in advance to ensure

133   hydraulic compliance with the anodic bonding sealing. Thus, theoretical ΔP value of 244 mbar

134   for 10 STP cm^3/min was calculated. It is noteworthy to underline that cavity depths varying from

135   20 μm to 120 μm were scrutinized by CFD simulations. In addition, preliminary breakthrough

136   tests, not shown here, revealed the existence of an optimal trade-off at 20 μm channel depth

137   which ensures efficient sorbate-sorbent contact at affordable pressure drop values for the

138   working conditions herein studied (flow rate and DMMP concentration).
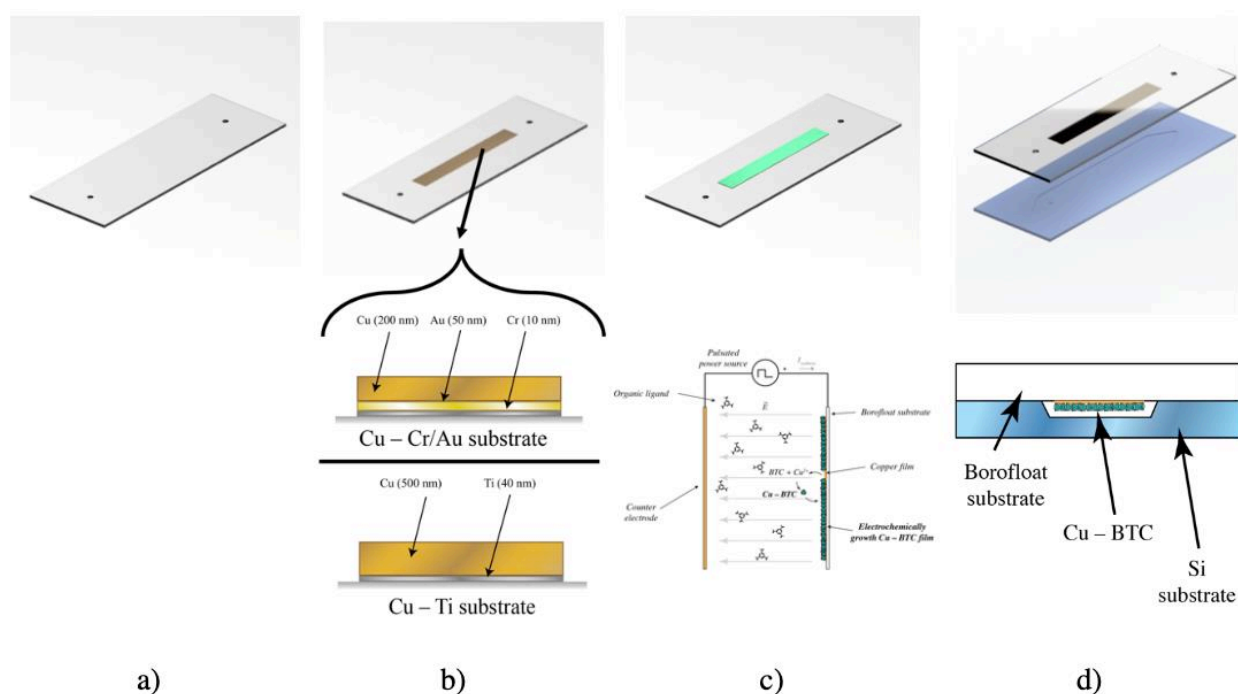
139

140   **Figure 1.** Main steps of the microdevice fabrication. a) Borofloat substrate. b) Cu based

141   deposition on Borofloat substrates (used as reference: Cu – Cr/Au and Cu – Ti substrates. c)

142   electrochemical synthesis of the Cu-BTC on Borofloat substrate. d) anodic bonding with Si

143   counterpart.

Synthesis and characterization of Cu-BTC films on Borofloat substrates

The electrosynthesis of Cu-BTC was carried out as previously reported (see Section 2 of the Supporting Information).[21] Using an Autolab potentiostat PGSTAT302N, cyclic pulses of different current (ranging from 1 to 15 mA) were applied between the Cu modified glass substrate used as working electrode and the counter-electrode. In this work, different electrosynthesis parameters were explored (Table 1) in order to maximize heterogeneous Cu-BTC crystallization, surface coverage and homogeneity. Very preliminary results, not shown here, performed with the same electrochemical cell revealed the existence of a minimum current density value, *i.e.* 1.5 mA/cm^2, for heterogeneous synthesis on Cu-Cr/Au modified glass substrates. Above this current density, an adequate concentration of Cu^{2+} ions, as net mass balance resulting from the generation term by Cu electrode oxidation and the consumption term by Cu-BTC formation, remains in the electrolyte solution for the successful nucleation and growth on the working electrode. Current duty cycle, *i.e.* on/off switching of applied current, was kept constant through all of the experiments (t_{cycle} = 20 s, duty cycle = 0.75, *i.e.* t_{on} = 15 s, t_{off} = 5s).

Cu-BTC coatings were firstly characterized by optical inspection supported by the turquoise (water coordinated state) color that Cu-BTC exhibits. SEM-EDX analyses (INSPECT-F50) were performed to determine the composition and morphology of the films. Purity and crystallinity of the Cu-BTC coatings were evaluated by surface X-ray diffraction (Bruker D8 Advance High Resolution Diffractometer) and XPS (Kratos Axis X-ray spectrometer).

Table 1. Electrosynthesis conditions studied in this work.

Substrate	Sample	$I_{synthesis}$	$J_{synthesis}$ (mA/cm^2)	N_{cycles}

				(mA)
Cu-Cr/Au	#1_12	1.0	1.6	12
	#2_12			12
	#2_15	9.0	17.3	15
	#2_20			20
	#3_12	15.0	28.8	12
Cu-Ti	#4_15*	6.0	8.7	15
	#5_7	12.0	17.4	7
	#5_15			15

* Conditions selected for the fabrication and testing of the functional microdevices studied in this work.

Adsorption properties of Cu-BTC

The textural properties of Cu-BTC films were assessed from Ar physisorption analysis, carried out on commercial Cu-BTC in powder form, Basolite C300, purchased from Sigma Aldrich. The as received bulk material was also used to quantify the adsorption properties towards DMMP when exposed to 3748 mg/m^3 of DMMP at 293 K (in dry air and at 30 % RH at 293K). Similar experiments were performed on previously activated samples (degassed overnight in an oven at 423 K and atmospheric pressure) to analyze the influence of water content on DMMP adsorption properties. An aliquot of the exposed MOF as well as of the activated material were taken and analyzed by thermogravimetry on a TA Instruments TGA-Q5000 (using N_2 up to 873 K at 10 K/min as heating rate). Quantification was performed using CuO as basis of calculation.

Theoretical adsorption isotherms have been calculated by combination of Monte Carlo (MC) simulations, in particular, by using the Metropolis–Hastings algorithm and molecular dynamics calculations based on UFF[23] as a force field.

181   Dynamic and equilibrium adsorption properties of the functional Cu-BTC μpreconcentrators as

182   well as uncoated counterparts, with and without micropatterned Cu electrode, have been

183   evaluated by breakthrough testing. The characteristic parameters: breakthrough time $t_{5\%}$;

184   breakthrough volume $V_{5\%}$; and dynamic sorption capacity W_d and equilibrium sorption capacity

185   W_{eq} were calculated from the analyses of breakthrough curves (see Section 3 of the Supporting

186   information for more details).

187   Breakthrough experiments were performed with concentrations of 162 mg/STP m^3 (32 ppmV)

188   of DMMP in dry N$_2$. For the remainder of this work, all the volumetric units refer to STP

189   conditions. In order to achieve a reliable and stable DMMP/N$_2$ stream, 10 cm^3/min of dry N$_2$ was

190   circulated through a calibrated permeation tube of DMMP (VALCO, permeation rate of 1629.96

191   ng/min ± 0.71% at 100 ºC) and fed directly to the μ-preconcentrator. The μ-devices were

192   connected upstream to the DMMP atmosphere generator and downstream to a GCMS (Shimadzu

193   GCMS-QP2010) through fused silica capillaries ($\varnothing_{capillary}$ = 320 μm) and 1/8" Teflon pipes. The

194   eluted gas concentration was sent to analyze each 60 s through a 500 μL sampling loop and the

195   characteristic DMMP fingerprint (u.m.a: 79, 94, 109 and 124) was quantified. The μ-

196   preconcentrator was reconditioned overnight at 473 K under 10 cm^3/min dry N$_2$ stream.

197   The preconcentration performance of the μ-device is evaluated from its preconcentration

198   coefficient, denoted as K [24]. This parameter mainly depends on the adsorbent type and loading,

199   the trapping efficiency, the number and nature of competing vapors in the sample and the sample

200   volume. According to IUPAC guidelines[25], this value is defined as the ratio of the air sample

201   collected volume to the volume in which that same mass is released according to the

202   quantification at the point of detection, assuming no transfer mass losses take place.

203   Accordingly, the K estimation is carried out under experimental conditions that guarantee the

204　absence of target molecules in the outlet stream, *i.e.* no breakthrough conditions.

205　Preconcentration experiments were performed with atmospheres of 2.64 mg/m^3 (520 ppbV) of

206　DMMP in dry N$_2$. As previously, atmospheres were generated by circulating 10 cm^3/min of dry

207　N$_2$ through a calibrated permeation tube of DMMP (VALCO, permeation rate of 148.41 ng/min

208　± 3.07 at 90 ºC) and fed to the μ-preconcentrator. The atmosphere was sampled for 10, 30 and 60

209　min at 298 K, after which the μ-device was firstly swept with 3 cm^3/min of the GCMS carrier

210　gas (He) for 5 min at room temperature and then at 473 K. The desorbed pulse of concentrated

211　DMMP was injected to GCMS. Further information on set-up configurations used on

212　breakthrough and preconcentration experiments can be found in Section 3 and Section 4 of the

213　Supporting Information.

214　**RESULTS AND DISCUSSION**

215　**Potentiometric working mode for Cu-BTC electrosynthesis: effect of current density**

216　Current density J plays a crucial role in electrosynthesis. This parameter governs the Cu

217　electrode oxidation rate; and consequently, the concentration of Cu^{2+} ions in the electrolyte

218　solution available for Cu-BTC crystallization. A pristine Cu-Cr/Au substrate as well as a

219　processed one were analyzed by energy-dispersive X-ray spectroscopy (EDS) to illustrate the

220　reactive Cu processes. As shown in Figure 2.a, the atomic analysis reveals an homogenous

221　distribution of Cu, Au and Cr layers, with a signal intensity proportional to layer thickness and

222　beam penetration (theoretical electron penetration of incident beam 427 nm for an accelerating

223　voltage of 10 kV on the Cu–Au/Cr substrate was calculated according to published work[26]).

224　After electrochemical synthesis, the mapping of C signal (mainly attributed to the organic linker)

225　correlates well with the distribution of Cu-BTC crystals over the substrate where the most

226　intense Cu signals are also recorded (Figure 2.b). In contrast, the Cu signal is clearly attenuated

227 on the naked surface in accordance to the lesser Cu thickness; whereas the Au and Cr signals are

228 proportionally increased.

a)   b)

c)
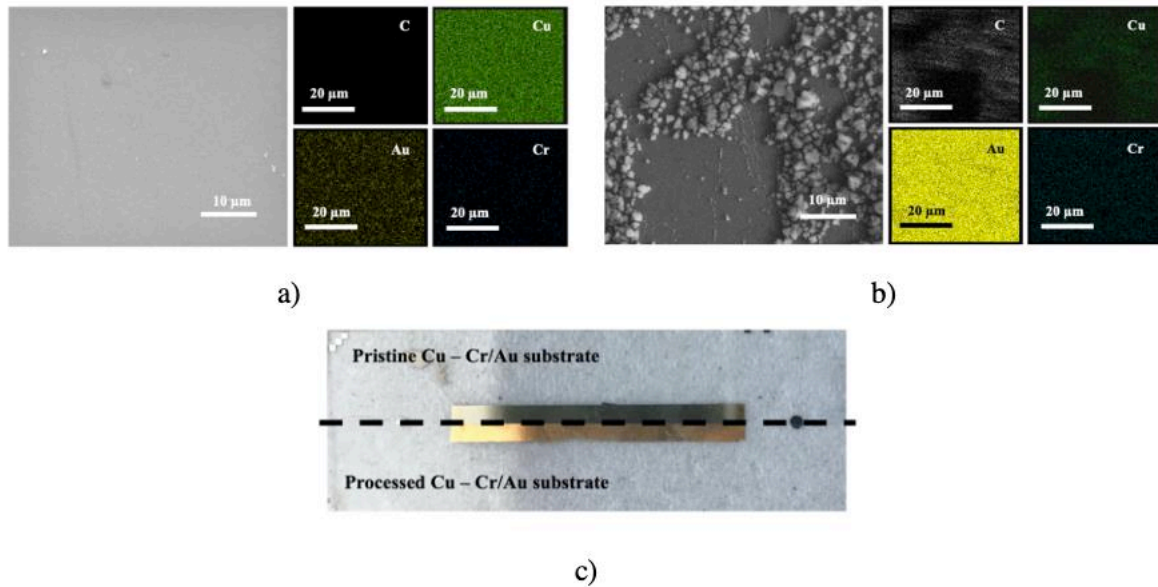
229

230 **Figure 2.** SEM-EDS results and visual inspection on Cu–Cr/Au substrates. a) pristine Cu–Cr/Au

231 substrate: on the left side a SEM micrograph of the analyzed area; on the right, from top to

232 bottom and left to right, the registered signals of C (white), Cu (green), Au (yellow) and Cr

233 (blue) on the centered area of the SEM micrograph. b) sample #2_20 ($J_{synthesis}$=17.3 mA/cm^2, 20

234 cycles): the images are displayed as previously. c) Composed image of the back side of Cu–

235 Cr/Au substrates before and after electrosynthesis under optimized conditions: $J_{synthesis}$ = 17.3

236 mA/cm^2, 15 cycles.

237   At current densities above 1.5 mA/cm^2, Cu-BTC crystallization begins to occur preferentially

238 at the borders of the metal electrode where the Gibbs free energy of the nucleation process is

239 decreased due to the presence of more grain boundary defects. By increasing the number of

240 cycles, the population of discrete Cu-BTC crystals grows rapidly all along the metal substrate,

241 but without forming a continuous and homogenous layer (Figure 3.a). At the highest current

242 density tested ($J_{synthesis}$ = 28.8 mA/cm^2), Cu-BTC layer formation is equally unsuccessful (Figure

243   3.c). This observation is attributed to the instability of the glass Cr/Au-Cu interface, more

244   pronounced at higher overpotentials (above 9 V) due to the electro-migration of Cr atoms into

245   the Au films (Figure 2.c).[27] In addition, the inter-diffusion of Cr into Au layers is temperature

246   dependent, i.e. solubility of Cr in Au at 323 K increases up to 5 atom %.[28] This mechanism

247   would provoke an unsteady current density distribution profile over the working Cu electrode

248   immersed in the electrolyte solution at 313 K resulting in a heterogeneous coverage of the

249   substrate. Among the tested conditions, the most homogeneous Cu-BTC coatings are attained at

250    $J_{synthesis}$ = 17.3 mA/cm^2 in a range of synthesis cycles from 10 to 20 (Figure 3.b). The

251   characteristic turquoise color of Cu-BTC is clearly noticed over the whole electrode surface. This

252   observation correlates well with the SEM analysis performed at random spots of the surface.
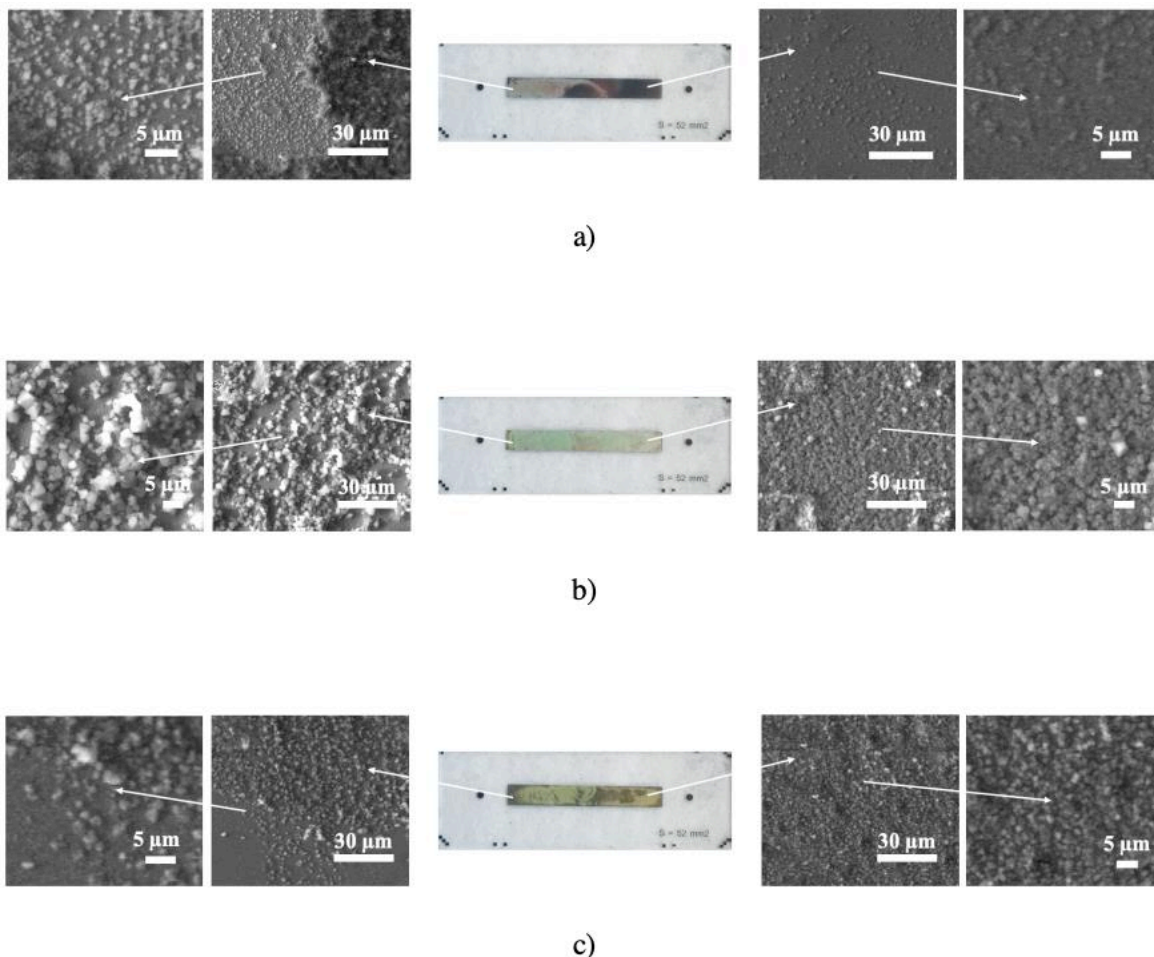
Figure 3. Electrochemical synthesis of Cu-BTC on Cu-Cr/Au substrates: a) sample #1_12: $J_{synthesis}$=1.6 mA/cm^2. b) #2_15: $J_{synthesis}$=17.3 mA/cm^2. c) #3_12: $J_{synthesis}$ = 28.8 mA/cm^2.

Cu-BTC electrosynthesis on Cu-Ti substrates

Cu-BTC electrosynthesis on Cu-Ti substrates was also investigated in order to overcome the instability issues of the glass-Cu interface due to chromium electromigration. As reported by Hsu et al.[29], titanium atoms do not tend to diffuse into Cu films and a well-defined Ti layer; and a stable Ti-Cu interface is commonly obtained. Unlike Cu-Cr/Au substrates, the Cu thickness in Cu-Ti substrates was increased up to 500 nm to ensure that Cu-BTC crystal growth is not eventually hindered by the concentration of Cu ions in the electrolyte solution. Likewise, the electrosynthesis parameters were slightly modified in accordance to the variations in the energy

14

264 required to overcome the electric resistance of the equivalent circuit, i.e. metal substrate –

265 reaction media – counter-electrode.

266 Figure 4 summarizes the characterization of sample #4_15, *i.e.* $J_{synthesis}$ = 8.6 mA/cm^2, N_{cycles}

267 =15. The visual inspection (Figure 4.a) clearly confirms the homogeneity of the continuous Cu-

268 BTC film 4.7 ± 1.1 µm thick, as measured by profilometry, equivalent to 113 ± 26 µg assuming

269 0.35 g/cm^3 as MOF density. The spatial EDS mappings of Cu and C atoms (Figure 4.b) clearly

270 overlap each other, whereas the Ti signal remains nearly constant, only slightly shielded where

271 agglomerated octahedral Cu-BTC crystals are encountered on the electrode surface. The

272 crystallinity of the supported Cu-BTC film was evaluated by XRD analysis. In Figure 4.c the

273 main characteristic Bragg reflections at small 2θ angles for HKUST-1 (2θ = 5.8º, 6.7º, 9.5º,

274 11.6º; corresponding to (111), (200), (220) and (222) crystallographic planes) are observed.[14]

275 Unlike the PXRD of commercial Cu-BTC, a preferential crystallographic orientation along the

276 [111] direction is observed for the electrosynthesized Cu-BTC film. In addition, the coexistence

277 of Cu_2O impurities, already present in the pristine Cu-Ti substrate (diffraction peaks at 38.3º and

278 43.5º [30]), is clearly noticed as commonly found in Cu-BTC synthesis.[31]

279 Although the XPS measurements give only a semiquantitative elemental composition, the

280 presence of C, O, Cu in the Cu-BTC coating was confirmed. The Cu 2p3/2 and Cu 2p1/2 lines,

281 found at the binding energies of 934.7 and 954.6eV are ascribed to the binding energy of Cu

282 2p3/2 and Cu 2p1/2, respectively, which are presented on Cu-BTC films.[32] The peaks of Cu

283 2p3/2 and Cu 2p1/2 are also de-convoluted into two components (see Figure 4.d). Thus, the

284 fittings of Cu 2p3/2 lead to binding energies of 932.6 and 934.7 eV, which correspond to surface

285 Cu+/Cuº and Cu2+ species, respectively. A quantitative analysis on the Cu 2p3/2 XPS spectra

286   gives rise to the surface $Cu2+/Cu+/0$ M ratio of 1.017. Similarly, the Cu 2p1/2 peak is de-

287   convoluted in two components at 952.7 and 954.5 eV.

288   In addition, there are three shake up satellite peaks, which are typical Cu2+ in cupric

289   compounds. These satellite peaks, on the high binding energy side of the core level Cu 2p XPS

290   data at 939.8, 944.1 and 963.1 eV, originate from multiple excitations in copper oxides and they

291   are known to be characteristics of CuO phase.[33] Therefore, the presence of the intense shake-up

292   satellite structures observed in the Cu 2p XPS spectra of D3 sample, accounting for circa 35% of

293   total copper content on the surface, was an indication of the simultaneous formation of Cu-BTC

294   and CuO phases, aon the surface of the electrosynthesized films.

295   The starting Cu/Ti electrode was also examined. Peaks at 932.8 eV (Cu 2p3/2) and 952 eV (Cu

296   2p1/2) and the absence of satellites shake-up lines characteristic of Cu2+ give clear evidence that

297   Cu is present in the+1 oxidation state, in agreement with the XRD spectra show in Figure 4.c.

298
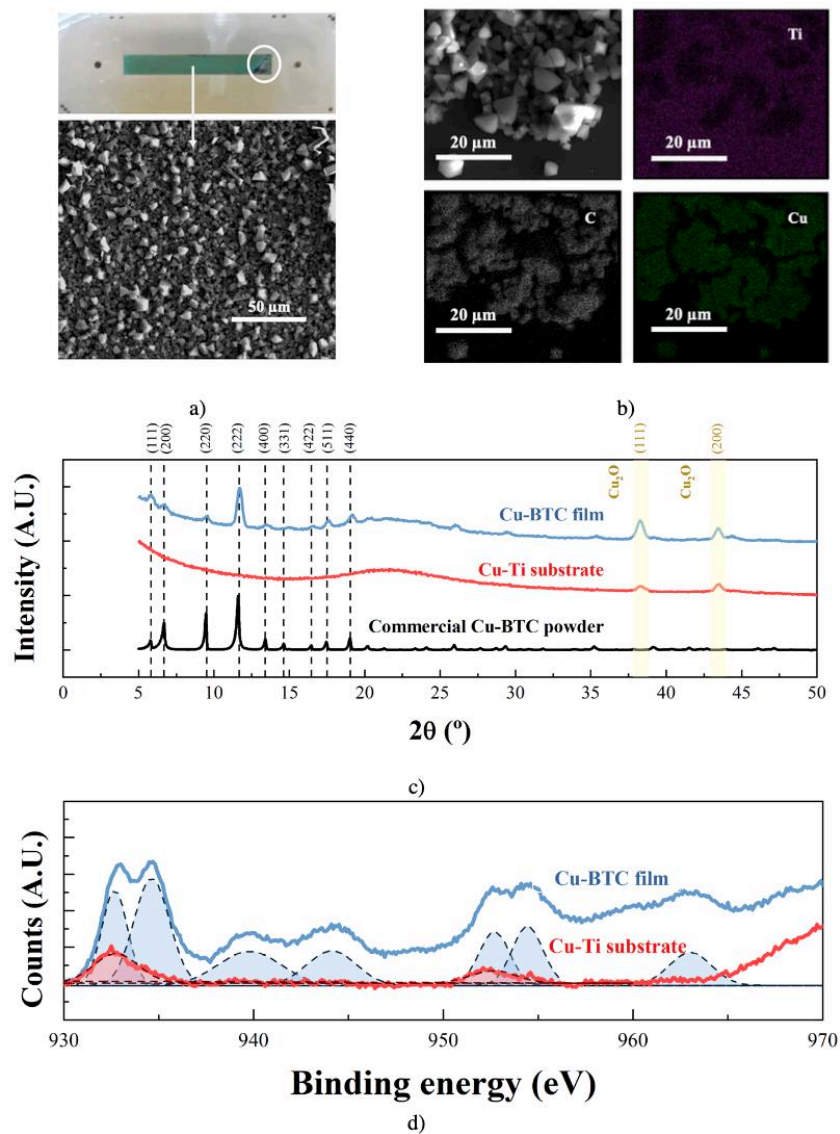
Figure 4. Electrochemical synthesis of Cu-BTC on Cu-Ti substrates: sample #4 ($J_{synthesis}$ = 8.6

mA/cm^2, N_{cycles} =15). a) Optical image, below SEM micrograph of a representative area of the

coating. b) SEM-EDS results on the clamping region highlighted in a), showing the overlapping

of Cu (green) and C (white) signals. c) XRDs of the Cu-BTC film (blue), pristine Cu-Ti substrate

(red) and commercial Cu-BTC powder (black). Crystallographic patterns from.[14] d) Core level

Cu2p XPS spectra of the Cu-BTC film (blue) and pristine Cu-Ti substrate (red).

305   Figure 5 shows the chronopotentiometric measurements with time on stream. This analysis is

306   revealed as a reliable characterization tool for the assessment on the heterogeneous Cu-BTC

307   crystallization process. A smooth increase of the electric potential difference across the working

308   and counter electrodes would be expected with electro synthesis time and number of cycles.

309   Assuming constant the electrolyte's and the counter-electrode's resistivity, this slight effect

310   would be explained by the evolving working electrode, which becomes more insulator with

311   synthesis time due to the lesser conductivity of Cu-BTC films ($\sigma_{Cu\text{-}BTC} < 3$ x 10^{-9} S/m vs. $\sigma_{Cu} =$

312   5.96 x 10^7 S/m).[34] Overlapped voltage signals are registered for #4_15 (1) and #4_15 (2)

313   samples, respectively; both prepared under identical conditions ($J_{synthesis} = 8.6$ mA/cm^2, $N_{cycles} =$

314   15). More specifically, the applied overpotential slightly increases from 4.1 V for the 1st cycle to

315   4.7 V in the 15th cycle in agreement with the controlled formation of homogeneous Cu-BTC

316   films. Accordingly, these conditions have been selected for the fabrication of the functional

317   microdevices for sampling and preconcentration of nerve agents (NAs) diluted in gaseous

318   streams.
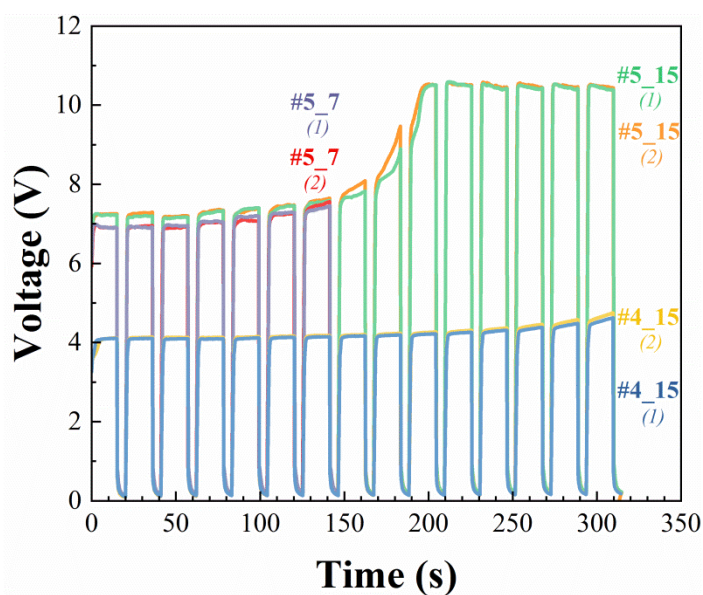
319

320   **Figure 5**. Chronopotentiometric analyses along the Cu-BTC electrosynthesis over Cu-Ti

321   substrates: #4_15 (1) in blue, #4_15 (2) in yellow, #5_7 (1) in purple, #5_7 (2) in red, #5_15(1)

322   in green and #5_15(2) in orange.

323   On the contrary, on samples #5_7 and #5_15, both at $J_{synthesis}$ = 17.4 mA/cm^2; the overpotential

324   evolution rate with time on stream is substantially higher from the 4th cycle and particularly

325   noticeable on 9th cycle. We attribute this observation to the detachment of the Cu-BTC layer

326   from the working electrode due to the exhaust of the Cu layer and the reduction of the

327   electroactive surface area.

328   **Water and DMMP adsorption properties of Cu-BTC powder**

329   Figure 6.a shows the characteristic Type I Ar isotherm at 87.3 K for commercial Cu-BTC. The

330   BET surface area is 1812 m^2/g (correlation coefficient of 0.9999). Micropore size distribution

331   has been modeled using nonlocal density functional theory (NLDFT) and considering cylinder

332   shape pore. The pore network of Cu-BTC has a simple cubic symmetry. It consists on a 3

333   dimensional channel system with main pores of ca. 9 Å and tetrahedral side pockets of ca. 5 Å.[35]

334   Such pore size distribution is illustrated in Figure 6.b with a total pore volume of 0.81 cm^3/g.

335   Cu-BTC is extremely sensitive to water content due to the very strong interaction between

336   open Cu(II) sites and water molecules.[27] TGA of the as received Cu-BTC is shown in Figure 6.c.

337   The first weight-loss up to 373 K accounts for 1216 mg/g$_{CuO}$ and it is mainly associated with

338   water content due to the relatively hydrophilic large pores. On the contrary, the water content of

339   activated samples is notably reduced, i.e. 150-175 mg/g$_{CuO}$ (Table 2). This observation highlights

340   the importance of the thermal activation to empty the framework efficiently.[36] The sample does

341   not show any significance weight change up to circa 523 K, onset temperature for the organic

342   linker degradation.

a)

b)

c)

d)

343
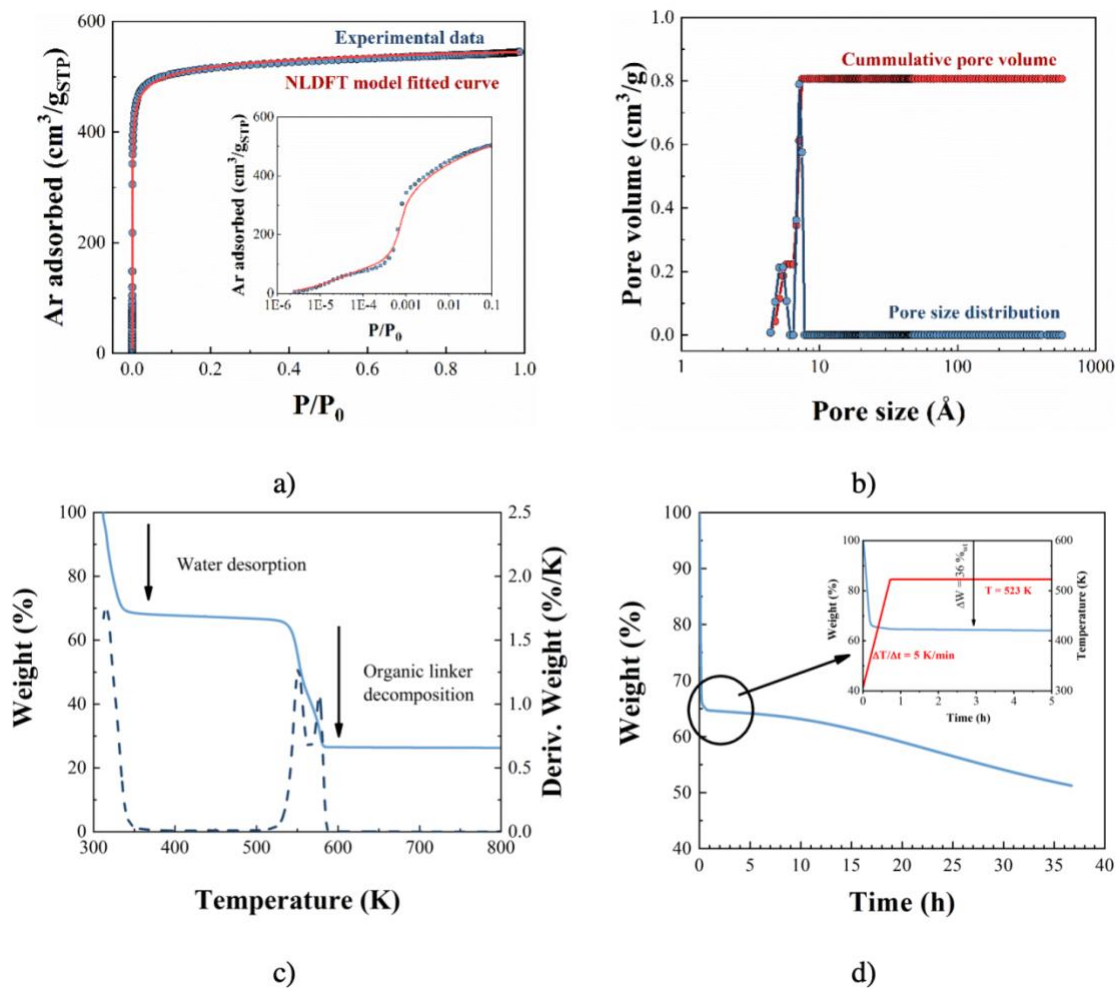
Figure 6. Textural characterization and TGA of commercial Cu-BTC (Basolite C300) a) Ar

adsorption isotherm (blue) and NLDFT model fitted curve (red). Insert: detail of low-pressure

region (0.0 < P/P0 < 0.1) of Ar adsorption isotherm (blue) and NLDFT fitted curve in

logarithmic scale. b) Pore volume distribution (blue) and cumulative pore volume (red)

according to NLDFT model assuming cylinder shape pore. (c) TGA (continuous line) and DTA

(discontinuous line) of as received sample. d) Thermal stability of as received sample at 523 K in

N_2 atmosphere for 36 h. Insert: detail for the first 5 h exposure time.

An aliquot of as received Cu-BTC sample was exposed to the fabrication process conditions to

assess the framework thermal stability during the anodic bonding, i.e. 523 K for 36 h (see Figure

353 6.d). A similar water weight loss is registered during the first heating ramp up to 523 K. During

354 the next 5 h at 523 K, no appreciable weight loss is recorded. Afterwards, the slope increases

355 gradually with time on stream. After 36 h exposure at 523 K, the weight loss due to the partial

356 degradation of the organic linker accounts for 11 %. Accordingly, the anodic bonding conditions,

357 523 K @ 1 kV, were kept for 5 h to preserve the Cu-BTC framework.

358 **Table 2**. DMMP adsorption on Cu-BTC at 293 K estimated by TGA

	Activated Cu-BTC		As received Cu-BTC	
	$\Delta m < 373\ K$ (mg/gCuO)	$\Delta m > 373\ K$ (mg/gCuO)	$\Delta m < 373\ K$ (mg/gCuO)	$\Delta m > 373\ K$ (mg/gCuO)
Control*	150	–	1216	–
DMMP (3748 mg/m3)	175	771	–	–
DMMP + Water (3748 mg/m3 + 7362 mg/m3)	238	297	323	267

359 *analyses on raw samples, without being exposed to DMMP or DMMP + water atmospheres

360

361 Table 2 comparatively shows the water and DMMP uptake values of activated Cu-BTC

362 samples for single DMMP *(DMMP@3748 mg/m³)* and binary DMMP + water mixture

363 *(DMMP@3748 mg/m³ + water@7362 mg/m³)* in N_2, respectively. The first weight-loss up to

364 373 K is attributed to water desorption, whereas those shown at temperatures above 373 K are

365 due to DMMP release. According to tabulated data, DMMP uptake is shown to be dependent on

366 the water content of the gas stream with a maximum DMMP sorption capacity of 771 mg/g$_{CuO}$ at

367 dry conditions. For single DMMP adsorption on activated samples, the differential thermogram

368 reveals the existence of three different sorption sites with different interaction energies (Figure

369   7.a). It is also found that most of the weight loss to DMMP desorption occurs at 433 K, Δm_{DMMP}

370   = 473.0 mg/g$_{CuO}$, vs. 112 mg/g$_{CuO}$ @ 500 K and 186 mg/g$_{CuO}$ @ 543 K. For the binary mixture

371   (Figure 7.b), the DMMP uptake of activated sample is notably reduced to less than half, i.e. 297

372   mg/g$_{CuO}$; and the triple peak that was seen before, no longer appears. This value is only slightly

373   superior to the quantified for co-adsorbed water vapor, i.e. 238 mg/g$_{CuO}$.
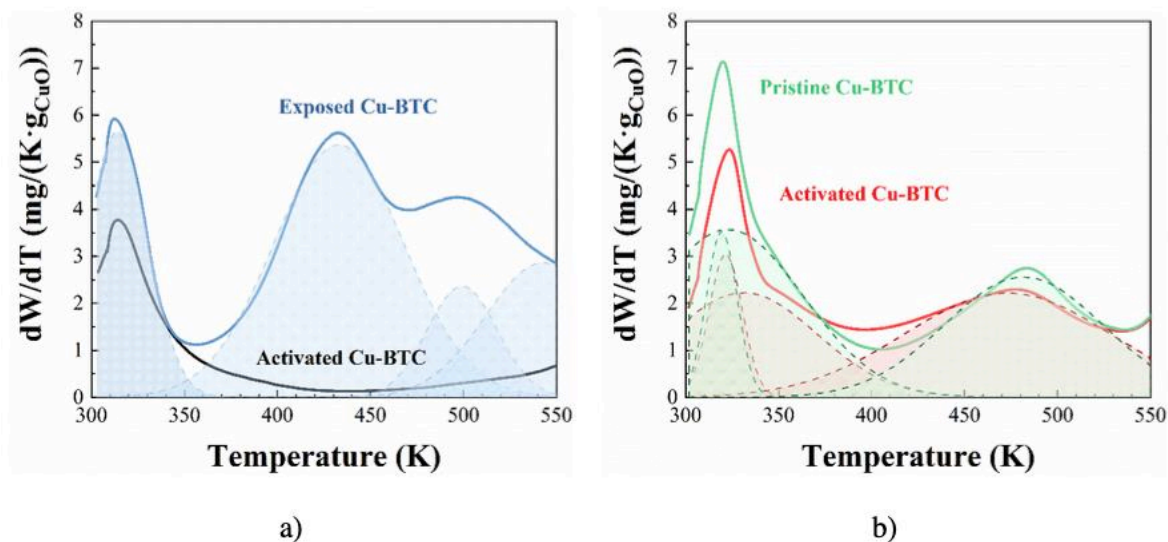
374   a)   b)

Figure 7. a) DTA of activated Cu-BTC before (black) and after exposure to 3748 mg/m^3 DMMP

376   in dry conditions (blue). Slashed blue lines depict de-convoluted peaks of exposed Cu-BTC. b)

377   DTA of activated Cu-BTC (red) and as received Cu-BTC (green) after co-exposure to DMMP

378   (3748 mg/m^3) and water (7362 mg/m^3). Slashed red and green lines depict de-convoluted peaks

379   of activated Cu-BTC (red) and as received Cu-BTC (green).

380   In "as received" Cu-BTC, the starting amount of pre-adsorbed water vapors (1216 mg/g$_{CuO}$)

381   has almost no influence on the final DMMP uptake in comparison with the activated sample: 267

382   mg/g$_{CuO}$ versus 297 mg/g$_{CuO}$. In both samples, a broad peak centered at 473 K associated to

383   DMMP desorption is observed in the differential thermograms. In other words, the binding

384   energy of DMMP- uncoordinated Cu(II) sites is lower in presence of co-adsorbed water vapor.

385 We attribute this effect to the formation of a DMMP-complex on the Cu(II) paddlewheels, where

386 the strong interaction of non-bridging phosphoryl oxygen atom in DMNP with uncoordinated

387 Cu(II) sites is attenuated due to proximity of water Cu(II) coordinated sites. Thus, the formation

388 of weaker hydrogen bonds between the hydroxyl groups present on the water Cu(II) coordinated

389 sites C and the P=O function of DMMP is softening the energy barrier for DMMP desorption. In

390 addition, the facilitated diffusion of desorbed DMMP molecules from the hydrated pores of Cu-

391 BTC is positively contributing due to the hydrophilic character of the surrogate. [37]

392 Moreover, water adsorption of as received Cu-BTC sample is reduced to almost a quarter in

393 presence of DMMP, i.e. 1216 mg/g$_{CuO}$ in non-competitive water adsorption scenario vs. 323

394 mg/g$_{CuO}$ for the binary mixture. Thus, the presence of DMMP in a competitive sorption scenario

395 is able to dehydrate the Cu-BTC sample and to allocate on active sites previously occupied by

396 water molecules.

397 The role of water inclusion in the physicochemical interactions for DMMP sorption within the

398 porous structure of Cu-BTC has been computationally studied to corroborate our hypothesis.

399 Low energy adsorption on surface sites of DMMP and water molecules on periodic Cu-BTC slab

400 built on different crystal orientations have been identified through Monte Carlo (MC)

401 simulations. In order to find minimal energy of the system, the temperature was modified

402 externally to simulate the annealing of the system from 100 K to 10^5 K for 20 cycles with 20000

403 of steps per cycle. The molecular interactions have been simulated by using UFF force field and

404 Ewald method as summation method. A similar study was performed on copper/copper oxides to

405 quantify the effect of the electrode and crystalline impurities.

406 Figure 8 shows the adsorption energies for DMMP in absence of co-adsorbed water vapor.

407 Crystal orientation of the simulated Cu-BTC slab plays an important role in DMMP surface

408 adsorption. Morphologies of the structures are also investigated (see Section 5 of Supporting

409 Information). The (110), (101), (011) and (111) orientations for Cu-BTC slabs show similar

410 appearance: oval-shape holes (13.2 Å x 18.6 Å). The (010) and (001) orientations present a

411 cross-shape trench of 6.5 Å, and the intersection of these trenches provides holes of 16.2 Å in

412 diameter. The (110), (101), (011) and preferential (111) crystallographic planes exhibit similar

413 adsorption energies, ca. -55 kcal/mol. On the contrary, the (010) and (001) orientations possess

414 two energy distribution probabilities centered at -51 kcal/mol and -73 kcal/mol, respectively.

415 Additionally, the average of adsorption energy for DMMP molecules adsorbed inside the Cu-

416 BTC micropores is lower than -30 kcal/mol. Such differences in the binding energies are

417 supporting the differential DMMP desorption profile shown in Figure 7.a. Thus, the broad peak

418 centered at 433 K would be attributed to the release of DMMP molecules from the Cu-BTC

419 micropores. The release of DMMP adsorbed on the surface seems to occur at higher temperature

420 due to strength of the interactions. The distribution of DMMP molecules on the available

421 sorption sites would explain the three desorption bands observed in the differential thermograms.
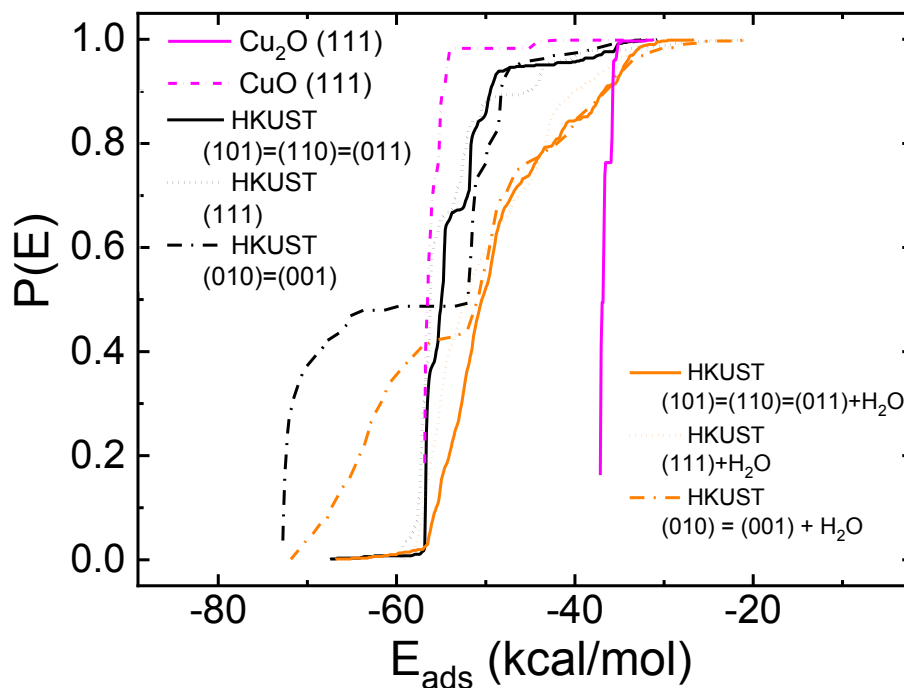
Figure 8. Montecarlo simulations of DMMP interactions over Cu-BTC and Cu_2O/CuO surfaces without and with co-adsorbed water vapor molecules.

Similarly, Figure 8 illustrates how the presence of co-adsorbed water vapor shifts the DMMP energy distribution probability to lower and more dispersed values. These simulations suggest that DMMP interactions with Cu-BTC surface become weaker in presence of co-adsorbed water vapor, supporting our hypothesis on the hydrogen bonding type interactions between the phosphoryl oxygen atom in DMMP and the hydroxyl groups present on the water Cu(II) coordinated sites.
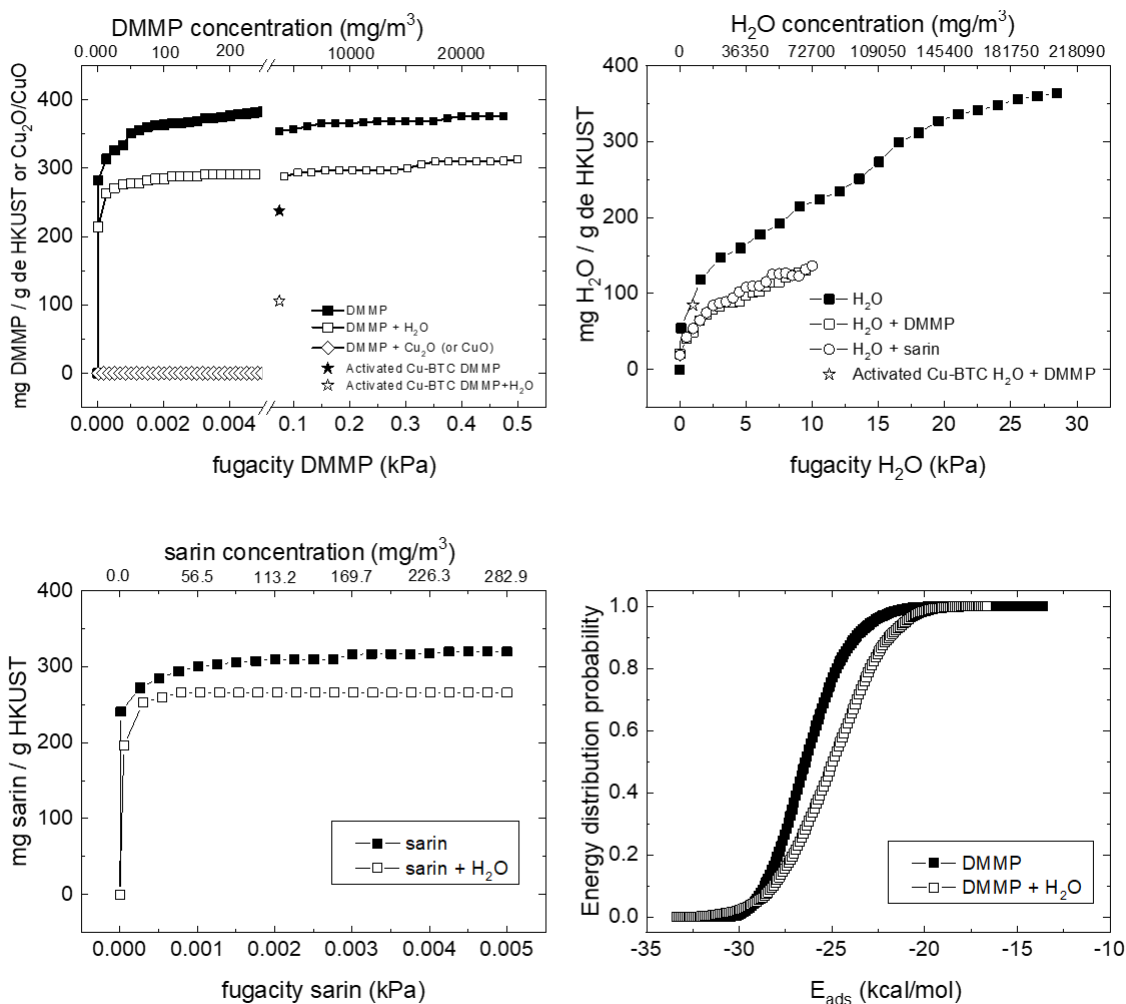
Figure 9. Simulated adsorption isotherms of DMMP, water and sarin gas at 298 K on Cu-BTC and Cu₂O/CuO surfaces and energy distribution probability for DMMP adsorbed inside the micropores for single and binary mixtures. The star-type symbols correspond to the experimental adsorption points shown in Table 2.

Figure 9 presents the calculated adsorption isotherms of DMMP, water and sarin gas on Cu-BTC microporosity at 298 K and the energy distribution probability for DMMP adsorbed inside pores in presence and absence of water. The discrete experimental points, shown in Table 2, are also included for comparison purposes. As it can be observed, the calculated values for Cu-BTC are superior to those experimentally obtained due to the presence of copper oxide impurities for

441 which the sorption properties are notably diminished due to their less surface area. For the

442 calculations 30000 steps and 1000000 production steps have been set on MC parameters. This

443 distribution correlates in same way than observed on case of surface adsorption. In general, the

444 adsorbate uptake values for single components are higher than those calculated for binary

445 mixtures (see Section 5 of Supporting Information). Thus, 73% of reduction for water uptake in

446 DMMP presence is recorded, a very similar value than obtained experimentally (70%). However,

447 DMMP shows a 20% of theoretically decay while experimentally shows a 61%. Our explanation

448 resides in the strong interactions of DMMP with the external surface which are underestimated in

449 the calculated isotherms, where only the molecules inside the micropores contribute to the

450 theoretical approximation. Furthermore, the predicted values for Sarin gas are rather similar to

451 those of DMMP analogue, supporting the suitability of Cu-BTC for Sarin gas detection.

452 **Performance of functional Cu-BTC μ-preconcentrators**

453 Breakthrough testing was performed on Cu-BTC functionalized μ-devices, denoted as

454 uPC_Cu-BTC, and also on analogues without MOF coating, denoted as uPC_Cu, for reference

455 purposes. In addition, a blank experiment with a sealed microdevice without micropatterned Cu

456 electrode (uPC_0) was carried out for baseline subtraction. The durability of the Cu-BTC

457 functionalized μ-devices were confirmed by assessment of the sorption properties upon exposure

458 to several sorption-desorption cycles of DMMP (see Section 6 of Supporting Information for

459 more details).

460 The breakthrough curves shown in Figure 10.a indicate that both uPC_Cu and uPC_Cu-BTC

461 material present close DMMP breakthrough time (3.2 min and 3.8 min respectively, thus 32 cm^3

462 and 38 cm^3 breakthrough volume at 162 mg/m^3). However, dynamic adsorption capacity is

463 higher in uPC_Cu-BTC than in uPC_Cu: 122.4 mg/g vs 41.7 mg/g. In fact, the adsorption rate –

464 which can be inferred by the slope of the breakthrough curve – is similar in both microdevices up

465 to values of 0.5 C_x/C_0. The estimated adsorbate-adsorbent interaction energy on CuO and Cu_2O

466 surfaces is -58 and -37 kcal/mol, respectively, as depicted in Figure 8. For the later one, the value

467 is lower than the analogue for any Cu-BTC surface but high enough to explain the experimental

468 behaviour. This adsorption occurs thanks to the formation of hydrogen bonds between the

469 hydroxyl groups present on the surface of CuO/Cu_2O concomitant phases dispersed over the Cu-

470 BTC film and the P=O function of DMMP.[38] Above all, this effect is hindered by the low surface

471 area of the copper oxides impurities. The simulated adsorption isotherms of DMMP on CuO and

472 Cu_2O structures (Figure 9) show an equilibrium value of almost zero indicating the adsorption of

473 DMMP over these oxides is only due to external surface interactions. From C_x/C_0 higher than

474 0.5, the adsorption rate notably decays on the Cu-BTC functionalized microdevices. Our

475 explanation relies on the saturation of the DMMP adsorption sites distributed on the external

476 surface. Thus, DMMP molecules, strongly adsorbed on the surface of the Cu_2O/Cu crystalline

477 impurities and those on the external surface of Cu-BTC crystals, start to diffuse inside the

478 microporous structure. In this adsorption regime, intra-crystalline diffusional limitations become

479 controlling although the adsorbate-adsorbent interactions within the micropores are less

480 energetic. Whereas uPC_Cu becomes saturated after sampling 772 cm^3 of DMMP/N_2, the higher

481 surface area of the Cu-BTC coating increases that volume up to 1541 cm^3. Overall, the

482 equilibrium adsorption capacity for DMMP is 691 mg/g for uPC_Cu-BTC @ 162 mg/m^3. This

483 DMMP uptake clearly overpasses standard adsorption materials such as active carbons (30.4

484 mg/g @ 230 mg/m^3) [39] or Tenax TA (39 mg/g @ 500 mg/m^3) [40]; as well as certain theoretical

485 values calculated for MOFs (e.g. MIP-177 @ 245 mg/g, UiO-66 @ 403 mg/g) [41].
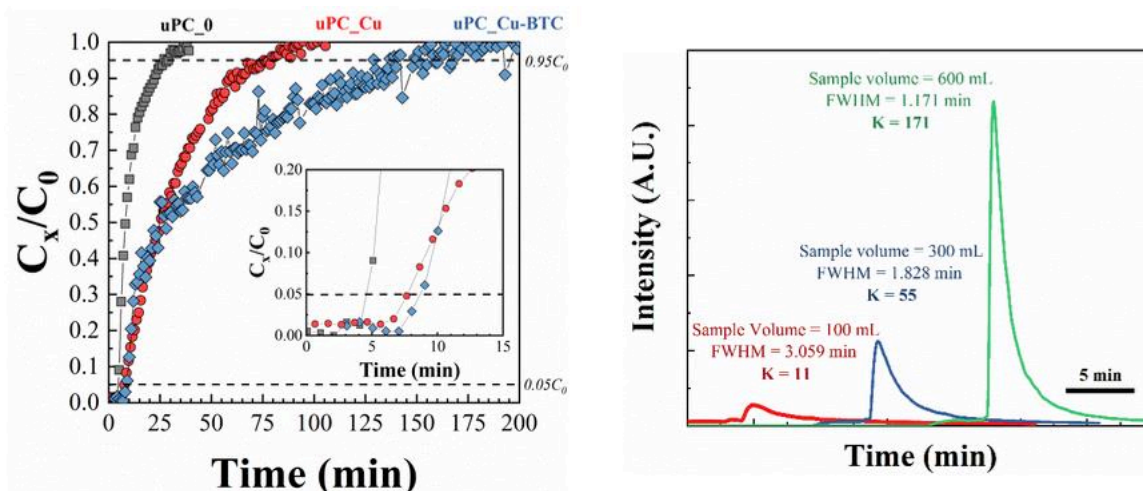
Figure 10. Performance of functional Cu-BTC μ-preconcentrators. a) Breakthrough testing for microdevices exposed to 162 mg/m^3 (32 ppmV) of DMMP 10 cm^3 /min dry N$_2$: without Cu electrode (black), without (red) and with Cu-BTC coating (blue). Insert: detail of the breakthrough curve. b) Preconcentration experiments with uPC_Cu-BTC for 2.64 mg/m3 (520 ppbV) of DMMP.

Finally, the preconcentration performance of the functional Cu-BTC microdevices is evaluated by means of the preconcentration coefficient, denoted as K. Previous dynamic experiments with the functionalized microdevices helped us to identify the operating window for a consistent K determination. The evolution of K for a sarin surrogate concentration of 2.64 mg/m^3 (520 ppbV) as a function of the sample volume, varying from 100 cm^3 to 600 cm^3, is illustrated in Figure 10.b. Assuming the entire release of the collected DMMP mass by thermal flushing at 473 K, the desorption volume is given by the carrier gas flow rate that sweeps the microdevice, i.e. 3 cm^3/min, and the full width at half maximum (FWHM) of the registered desorption peak (see Section 4 of the Supporting Information for more details). There is a linear correlation between K and sample volume, i.e., higher values of K are observed at higher sample

29

502 volume in agreement with published literature.[42] The maximum K is 171 and corresponds to

503 half-maximum injection peak width of ~1 min after collecting 1584 ng of DMMP (V_{sample} =

504 600 cm^3). Such preconcentration coefficient would require 60 min of sampling at 10 cm^3/min. It

505 must be emphasized; however, that similar breakthrough volumes and K values are attained at

506 higher sampling rates, i.e. 100 cm^3/min, for microfluidic cavities 40 μm depth at the expense of

507 higher hydraulic losses. Thus, the latter time period may be reduced to 6 min, more suitable for

508 some applications requiring shorter analytical duty cycles. Analogous experiments carried out

509 with μPC_Cu device, not shown here, did not succeed due to their dynamic sorption values were

510 almost null at these experimental conditions.

511 Accordingly, quantitative "on field" determination of NAs could be realized by coupling this

512 functional Cu-BTC μ-preconcentrator to downstream Surface Enhanced Raman Spectroscopy

513 (SERS) based sensor with a DMMP detection limit as low as 130 ppbV and 100 s of response

514 time, already developed in our group.[43,44] Considering the Sarin acute exposure guideline level

515 (AEGL-3) of 64 ppbV for an exposure of 10 min,[3] i.e. the persons expose above this

516 concentration for this period could experience life-threatening health effects or death, the

517 combined Cu-BTC μ-preconcentrator + SERS unit would enable the rapid identification of Sarin

518 when present at concentrations below the threshold AEGL3 value.

519 **CONCLUSIONS**

520 The results presented in this work confirm the integration of homogenous Cu-BTC films on

521 microdevices via electrochemical assisted synthesis. We have identified the adequate synthesis

522 conditions that lead to reproducible MOF coatings of circa 5 μm thick: Cu (500 nm). Activated

523 Cu-BTC powder samples exhibit high adsorption capacity towards DMMP, i.e. 771 mg/g$_{CuO}$ at

524 293 K and 3748 mg/m^3, which overpassed other commercial adsorbents. The DMMP uptake of

525 Cu-BTC samples exposed to DMMP+water binary mixtures is equally noteworthy. Despite the

526 high hydrophilicity of this material (1216 mg_{H2O}/g_{CuO} at 293 K and 7362 mg/m^3 of water), the

527 DMMP adsorption capacity remains remarkable even for humid conditions: above 250 mg/g_{CuO}

528 at 293 K and 3718 mg/m^3 of DMMP. In fact, the adsorption of DMMP molecules on the less

529 energetic hydrophilic sites seems to be facilitated in presence of co-adsorbed water vapor in

530 agreement with computational studies. These results are supporting the "on field" application of

531 functional Cu-BTC microdevices as reliable µ-preconcentrators for nerve agents.

532 The functional Cu-BTC based µ-preconcentrators exhibit equilibrium DMMP adsorption

533 capacities up to 690 mg/g at 298 K and 162 mg/m^3 (32 ppmV), clearly superior to published data

534 on organophosphorous compounds. A preconcentration coefficient of 171 is determined for

535 sample volume of 600 cm^3 containing 2.68 mg/m^3 (520 ppbV). These promising results pave the

536 way for further development of microsystems comprising micropreconcentrator and SERS based

537 sensors capable of quantitative determination of NAs under field conditions.

538 **ASSOCIATED CONTENT**

539 **Supporting Information**

540 The Supporting Information is available free of charge on the ACS Publication website at DOI:

541 XXXXXXXXX.

542 Fabrication of µ-preconcentrators (Section 1), experimental set-up for the electrochemical

543 synthesis on Cu modified glass substrates (Section 2), breakthrough testing of functional

544 preconcentrators (Section 3), experimental set-up for preconcentration factor determination

545 (Section 4), morphologies of the structures used for Montecarlo simulations (Section 4).

546 **AUTHOR INFORMATION**

547 **Corresponding Author**

548   *E–mail: mapina@unizar.es (M.P.P.)

ORCID

Fernando Almazan: 0000-0001-5063-2987

Miguel A. Urbiztondo: 0000-0002-4931-1358

Pablo Serra-Crespo: 0000-0002-5106-0527

Beatriz Seoane: 0000-0002-9100-4773

Jorge Gascon: 0000-0001-7558-7123

Jesus Santamaria: 0000-0002-8701-9745

M. Pilar Pina: 0000-0001-9897-6527

Author Contributions

The manuscript was written through contributions of all authors. All authors have given approval to the final version of the manuscript.

Funding Sources

Notes

The authors declare no competing financial interests.

REFERENCES

(1) Newmark, J. Nerve Agents. *Neurologist* **2007**, *13* (1), 20–32. https://doi.org/10.1097/01.nrl.0000252923.04894.53.

(2) John, H.; van der Schans, M. J.; Koller, M.; Spruit, H. E. T.; Worek, F.; Thiermann, H.; Noort, D. Fatal Sarin Poisoning in Syria 2013: Forensic Verification within an International Laboratory Network. *Forensic Toxicol.* **2018**, *36* (1), 61–71. https://doi.org/10.1007/s11419-017-0376-7.

(3) US EPA, O. Agent GB (Sarin) Results - AEGL Program.

(4) Leidinger, M.; Rieger, M.; Sauerwald, T.; Alépée, C.; Schütze, A. Integrated Pre-Concentrator Gas Sensor Microsystem for Ppb Level Benzene Detection. *Sensors Actuators, B Chem.* **2016**, *236*. https://doi.org/10.1016/j.snb.2016.04.064.

(5) Gregis, G.; Sanchez, J.-B.; Bezverkhyy, I.; Guy, W.; Berger, F.; Fierro, V.; Bellat, J.-P.; Celzard, A. Detection and Quantification of Lung Cancer Biomarkers by a Micro-Analytical Device Using a Single Metal Oxide-Based Gas Sensor. *Sensors Actuators B Chem.* **2018**, *255*, 391–400. https://doi.org/https://doi.org/10.1016/j.snb.2017.08.056.

(6) Bang, J.; You, D.-W.; Jang, Y.; Oh, J.-S.; Jung, K.-W. A Carbon Nanotube Sponge as an

589   Adsorbent for Vapor Preconcentration of Aromatic Volatile Organic Compounds. *J.*

590   *Chromatogr.*   *A*   **2019**,   460363.

591   https://doi.org/https://doi.org/10.1016/j.chroma.2019.460363.

592   (7)   Ni, Z.; Jerrell, J. P.; Cadwallader, K. R.; Masel, R. I. Metal-Organic Frameworks as

593   Adsorbents for Trapping and Preconcentration of Organic Phosohonates. *Anal. Chem.*

594   **2007**, *79* (4), 1290–1293. https://doi.org/10.1021/ac0613075.

595   (8)   Montoro, C.; Linares, F.; Quartapelle Procopio, E.; Senkovska, I.; Kaskel, S.; Galli, S.;

596   Masciocchi, N.; Barea, E.; Navarro, J. A. R. Capture of Nerve Agents and Mustard Gas

597   Analogues by Hydrophobic Robust MOF-5 Type Metal-Organic Frameworks. *J. Am.*

598   *Chem. Soc.* **2011**, *133* (31), 11888–11891. https://doi.org/10.1021/ja2042113.

599   (9)   Carrillo, C.; Martínez, G.; Julián, I.; Pina, M. P.; Mallada, R. Adsorción e Hidrólisis de

600   Compuestos Organofosforados Con MOFs Basados En Zr. In *VII Congreso Nacional de*

601   *I+D en Defensa y Seguridad*; 2019.

602   (10)   Ma, K.; Islamoglu, T.; Chen, Z.; Li, P.; C. Wasson, M.; Chen, Y.; Wang, Y.; W. Peterson,

603   G.; H. Xin, J.; K. Farha, O. Scalable and Template-Free Aqueous Synthesis of Zirconium-

604   Based Metal–Organic Framework Coating on Textile Fiber. *J. Am. Chem. Soc.* **2019**, *141*

605   (39), 15626–15633. https://doi.org/10.1021/jacs.9b07301.

606   (11)   Crooks, R. M. Interactions between Self-Assembled Monolayers and an

607   Organophosphonate. *Situ* **1997**.

608   (12)   Montoro, C.; Procopio, E. Q.; Senkovska, I.; Kaskel, S.; Galli, S.; Masciocchi, N.; Barea,

609   E.; Navarro, J. a R.; Linares, F.; Quartapelle Procopio, E. Capture of Nerve Agents and

Mustard Gas Analogues by Hydrophobic Robust MOF-5 Type Metal-Organic Frameworks. *J. Am. Chem. Soc.* **2011**, *133* (31), 11888–11891. https://doi.org/10.1021/ja2042113.

(13) Agrawal, M.; Sava Gallis, D. F.; Greathouse, J. A.; Sholl, D. S. How Useful Are Common Simulants of Chemical Warfare Agents at Predicting Adsorption Behavior? *J. Phys. Chem. C* **2018**, *122* (45), 26061–26069. https://doi.org/10.1021/acs.jpcc.8b08856.

(14) Chui, S. S.-Y.; Lo, S. M.-F.; Charmant, J. P. H.; Orpen, A. G.; Williams, I. D. A Chemically Functionalizable Nanoporous Material [Cu<Sub>3</Sub>(TMA)<Sub>2</Sub>(H<Sub>2</Sub>O)<Sub>3</Sub>]<Sub><Em>N</Em></Sub> *Science (80-.).* **1999**, *283* (5405), 1148 LP – 1150. https://doi.org/10.1126/science.283.5405.1148.

(15) Bétard, A.; Fischer, R. Metal-Organic Framework Thin Films: From Fundamentals to Applications. *Chem. Rev.* **2011**, *112*, 1055–1083. https://doi.org/10.1021/cr200167v.

(16) Drobek, M.; Bechelany, M.; Vallicari, C.; Abou Chaaya, A.; Charmette, C.; Salvador-Levehang, C.; Miele, P.; Julbe, A. An Innovative Approach for the Preparation of Confined ZIF-8 Membranes by Conversion of ZnO ALD Layers. *J. Memb. Sci.* **2015**, *475*, 39–46. https://doi.org/10.1016/j.memsci.2014.10.011.

(17) Carbonell, C.; Stylianou, K. C.; Hernando, J.; Evangelio, E.; Barnett, S. A.; Nettikadan, S.; Imaz, I.; Maspoch, D. Femtolitre Chemistry Assisted by Microfluidic Pen Lithography. *Nat. Commun.* **2013**, *4* (1), 2173. https://doi.org/10.1038/ncomms3173.

631   (18)   Cai, S.; Li, W.; Xu, P.; Xia, X.; Yu, H.; Zhang, S.; Li, X. In Situ Construction of Metal–

632   Organic Framework (MOF) UiO-66 Film on Parylene-Patterned Resonant Microcantilever

633   for Trace Organophosphorus Molecules Detection. *Analyst* **2019**, *144* (12), 3729–3735.

634   https://doi.org/10.1039/C8AN02508H.

635   (19)   Sachdeva, S.; Pustovarenko, A.; Sudhölter, E. J. R.; Kapteijn, F.; De Smet, L. C. P. M.;

636   Gascon, J. Control of Interpenetration of Copper-Based MOFs on Supported Surfaces by

637   Electrochemical   Synthesis.   *CrystEngComm*   **2016**,   *18*   (22),   4018–4022.

638   https://doi.org/10.1039/c5ce02462e.

639   (20)   Martinez Joaristi, A.; Juan-Alcañiz, J.; Serra-Crespo, P.; Kapteijn, F.; Gascon, J.

640   Electrochemical Synthesis of Some Archetypical Zn2+, Cu2+, and Al3+metal Organic

641   Frameworks.   *Cryst.   Growth   Des.*   **2012**,   *12*   (7),   3489–3498.

642   https://doi.org/10.1021/cg300552w.

643   (21)   Sachdeva, S.; Venkatesh, M. R.; Mansouri, B. El; Wei, J.; Bossche, A.; Kapteijn, F.;

644   Zhang, G. Q.; Gascon, J.; de Smet, L. C. P. M.; Sudhölter, E. J. R. Sensitive and

645   Reversible Detection of Methanol and Water Vapor by In Situ Electrochemically Grown

646   CuBTC MOFs on Interdigitated Electrodes. *Small* **2017**, *13* (29), 1604150.

647   https://doi.org/10.1002/smll.201604150.

648   (22)   Almazán, F.; Pellejero, I.; Morales, A.; Urbiztondo, M. A.; Sesé, J.; Pina, M. P.;

649   Santamaría, J. Zeolite Based Microconcentrators for Volatile Organic Compounds

650   Sensing at Trace-Level: Fabrication and Performance. *J. Micromechanics*

651   *Microengineering* **2016**, *26* (8), 084010. https://doi.org/10.1088/0960-1317/26/8/084010.

652   (23)   Rappé, A. K.; Casewit, C. J.; Colwell, K. S.; Goddard, W. A.; Skiff, W. M. UFF, a Full

Periodic Table Force Field for Molecular Mechanics and Molecular Dynamics Simulations. *J. Am. Chem. Soc.* **1992**, *114* (25), 10024–10035. https://doi.org/10.1021/ja00051a040.

(24) Serrano, G.; Sukaew, T.; Zellers, E. T. Hybrid Preconcentrator/Focuser Module for Determinations of Explosive Marker Compounds with a Micro-Scale Gas Chromatograph. *J. Chromatogr. A* **2013**, *1279*, 76–85. https://doi.org/10.1016/j.chroma.2013.01.009.

(25) Jackwerth, E.; … A. M.-P. A.; 1979, undefined. SEPARATION AND PRECONCENTRATION OF TRACE SUBSTANCES. 1. PRECONCENTRATION FOR INORGANIC TRACE ANALYSIS. *BLACKWELL Sci. LTD ….*

(26) Kanaya, K.; Okayama, S. Penetration and Energy-Loss Theory of Electrons in Solid Targets. *J. Phys. D. Appl. Phys.* **1972**, *5* (1), 43–58. https://doi.org/10.1088/0022-3727/5/1/308.

(27) Koleshko, V. M.; Kiryushin, I. V. Electromigration Threshold of Thin-Film Conductors. *Thin Solid Films* **1990**, *192* (1), 181–191. https://doi.org/https://doi.org/10.1016/0040-6090(90)90490-5.

(28) Todeschini, M.; Bastos da Silva Fanta, A.; Jensen, F.; Wagner, J. B.; Han, A. Influence of Ti and Cr Adhesion Layers on Ultrathin Au Films. *ACS Appl. Mater. Interfaces* **2017**, *9* (42), 37374–37385. https://doi.org/10.1021/acsami.7b10136.

(29) Hsu, S.; Chen, H.; Chen, K. Cosputtered Cu/Ti Bonded Interconnects With a Self-Formed Adhesion Layer for Three-Dimensional Integration Applications. *IEEE Electron Device Lett.* **2012**, *33* (7), 1048–1050. https://doi.org/10.1109/LED.2012.2194769.

674   (30)   Cheng, S.-L.; Chen, M.-F. Fabrication, Characterization, and Kinetic Study of Vertical

675   Single-Crystalline CuO Nanowires on Si Substrates. *Nanoscale Res. Lett.* **2012**, *7* (1), 119.

676   https://doi.org/10.1186/1556-276X-7-119.

677   (31)   Worrall, S. D.; Bissett, M. A.; Hill, P. I.; Rooney, A. P.; Haigh, S. J.; Attfield, M. P.;

678   Dryfe, R. A. W. Metal-Organic Framework Templated Electrodeposition of Functional

679   Gold Nanostructures. *Electrochim. Acta* **2016**, *222*, 361–369.

680   https://doi.org/https://doi.org/10.1016/j.electacta.2016.10.187.

681   (32)   Yang, Y.; Dong, H.; Wang, Y.; He, C.; Wang, Y.; Zhang, X. Synthesis of Octahedral like

682   Cu-BTC Derivatives Derived from MOF Calcined under Different Atmosphere for

683   Application in CO Oxidation. *J. Solid State Chem.* **2018**, *258* (September 2017), 582–587.

684   https://doi.org/10.1016/j.jssc.2017.11.033.

685   (33)   Akgul, F. A.; Akgul, G.; Yildirim, N.; Unalan, H. E.; Turan, R. Influence of Thermal

686   Annealing on Microstructural, Morphological, Optical Properties and Surface Electronic

687   Structure of Copper Oxide Thin Films. *Mater. Chem. Phys.* **2014**, *147* (3), 987–995.

688   https://doi.org/10.1016/j.matchemphys.2014.06.047.

689   (34)   Alfè, M.; Gargiulo, V.; Lisi, L.; Di Capua, R. Synthesis and Characterization of

690   Conductive Copper-Based Metal-Organic Framework/Graphene-like Composites. *Mater.*

691   *Chem. Phys.* **2014**, *147* (3), 744–750.

692   https://doi.org/https://doi.org/10.1016/j.matchemphys.2014.06.015.

693   (35)   Chen, Y.; Mu, X.; Lester, E.; Wu, T. High Efficiency Synthesis of HKUST-1 under Mild

694   Conditions with High BET Surface Area and CO2 Uptake Capacity. *Prog. Nat. Sci.*

695   *Mater. Int.* **2018**, *28* (5), 584–589. https://doi.org/10.1016/J.PNSC.2018.08.002.

696 (36) Schlichte, K.; Kratzke, T.; Kaskel, S. Improved Synthesis, Thermal Stability and Catalytic

697   Properties of the Metal-Organic Framework Compound Cu3(BTC)2. *Microporous*

698   *Mesoporous   Mater.   **2004**,   *73*   (1),   81–88.*

699   https://doi.org/https://doi.org/10.1016/j.micromeso.2003.12.027.

700 (37) Roy, A.; Srivastava, A. K.; Singh, B.; Shah, D.; Mahato, T. H.; Gutch, P. K.; Halve, A. K.

701   Degradation of Sarin, DEClP and DECNP over Cu-BTC Metal Organic Framework. *J.*

702   *Porous Mater.* **2013**, *20* (5), 1103–1109. https://doi.org/10.1007/s10934-013-9692-4.

703 (38) Schlur, L.; Agostini, P.; Thomas, G.; Gerer, G.; Grau, J.; Spitzer, D. Detection of

704   Organophosphorous Chemical Agents with CuO-Nanorod-Modified Microcantilevers.

705   *Sensors (Switzerland)* **2020**, *20* (4). https://doi.org/10.3390/s20041061.

706 (39) Vu, A. T.; Ho, K.; Lee, C. H. Removal of Gaseous Sulfur and Phosphorus Compounds by

707   Carbon-Coated Porous Magnesium Oxide Composites. *Chem. Eng. J.* **2016**, *283*, 1234–

708   1243. https://doi.org/10.1016/j.cej.2015.08.083.

709 (40) Han, Q.; Yang, L.; Liang, Q.; Ding, M. Three-Dimensional Hierarchical Porous Graphene

710   Aerogel for Efficient Adsorption and Preconcentration of Chemical Warfare Agents.

711   *Carbon N. Y.* **2017**, *122*, 556–563. https://doi.org/10.1016/j.carbon.2017.05.031.

712 (41) Soares, C. V.; Leitão, A. A.; Maurin, G. Computational Evaluation of the Chemical

713   Warfare Agents Capture Performances of Robust MOFs. *Microporous Mesoporous*

714   *Mater.* **2019**, *280*, 97–104. https://doi.org/10.1016/J.MICROMESO.2019.01.046.

715 (42) Bryant-Genevier, J.; Zellers, E. T. Toward a Microfabricated Preconcentrator-Focuser for

716   a Wearable Micro-Scale Gas Chromatograph. *J. Chromatogr. A* **2015**, *1422*, 299–309.

717 https://doi.org/10.1016/J.CHROMA.2015.10.045.

718 (43) Lafuente, M.; Pellejero, I.; Sebastián, V.; Urbiztondo, M. A.; Mallada, R.; Pina, M. P.;

719 Santamaría, J. Highly Sensitive SERS Quantification of Organophosphorous Chemical

720 Warfare Agents: A Major Step towards the Real Time Sensing in the Gas Phase. *Sensors*

721 *Actuators B Chem.* **2018**, *267*, 457–466.

722 https://doi.org/https://doi.org/10.1016/j.snb.2018.04.058.

723 (44) Lafuente, M.; Almazan, F.; Bernad, E.; Urbiztondo, M. A.; Santamaria, J.; Mallada, R.;

724 Pina, M. P. SERS Detection of Neurotoxic Agents in Gas Phase Using Microfluidic Chips

725 Containing Gold-Mesoporous Silica as Plasmonic-Sorbent. In *2019 20th International*

726 *Conference on Solid-State Sensors, Actuators and Microsystems and Eurosensors XXXIII,*

727 *TRANSDUCERS 2019 and EUROSENSORS XXXIII*; 2019.

728 https://doi.org/10.1109/TRANSDUCERS.2019.8808289.

729

730

731

732

733

734

735

For Table of Contents Only

Fabrication Approach

Borofloat substrate | Cu-Ti substrate deposition | Cu-BTC electrochemical growth

Silicon substrate | Chemical etching

Envisioned Application

H_2O

portable detection system

Preconcentration unit $\times 10^2$-10^3

Working principle

1st stage: capture

inlet → H_2O → oulet

normal situation — CuBTC

inlet → oulet

alarm situation — CuBTC

2nd stage: bolus desorption

Heating

Detector Response (a.u.)

"+"

"-"

SUPPORTING INFORMATION

Cu-BTC functional microdevices as smart tools for capture and preconcentration of nerve agents

F. Almazán,[1, 2] M.A. Urbiztondo [2, 3] P. Serra Crespo,[4] B. Seoane,[5] J. Gascon, [5,6] J. Santamaría,[1,7] M.P. Pina[1,7]*

[1] Instituto de Nanociencia y Materiales de Aragón (INMA), CSIC-Universidad de Zaragoza, Zaragoza 50009, Spain.

[2] Department of Chemical & Environmental Engineering, Campus Rio Ebro, C/Mariano Esquillor s/n, 50018 Zaragoza, Spain

[3] Centro Universitario de la Defensa de Zaragoza, Carretera Huesca s/n, 50090 Zaragoza, Spain

[4] Applied Radiation and Isotopes, Department of Radiation Science and Technology, Faculty of Applied Sciences, Technical University Delft, Mekelweg 15, 2629 JB, Delft, the Netherlands

[5] Catalysis Engineering, Department of Chemical Engineering, Delft University of Technology, Van der Maasweg 9, 2629 HZ Delft, The Netherlands

[6] Advanced Catalytic Materials, KAUST Catalysis Center, King Abdullah University of Science and Technology, Thuwal 23955, Saudi Arabia

[7] Networking Research Center on Bioengineering, Biomaterials and Nanomedicine, CIBER-BBN, 28029 Madrid, Spain

*Corresponding Author. E-mail: mapina@unizar.es

TABLE OF CONTENTS

Section S1. Fabrication of micropreconcentrators

Fabrication process is divided in five different steps: cavity etching, adsorbent incorporation, microdevice sealing, heater element integration and inlet/outlet ports mechanization (Figure S1).

Cavity etching is the first step performed to fabricate the microdevice. It is divided in to two steps: 1) photoresist deposition, 2) etching and 3) photoresist removal. For the simple geometries as well as large features (>100 µm) and deep cavities (> 20 µm) studied in this work, wet etching with KOH was used.
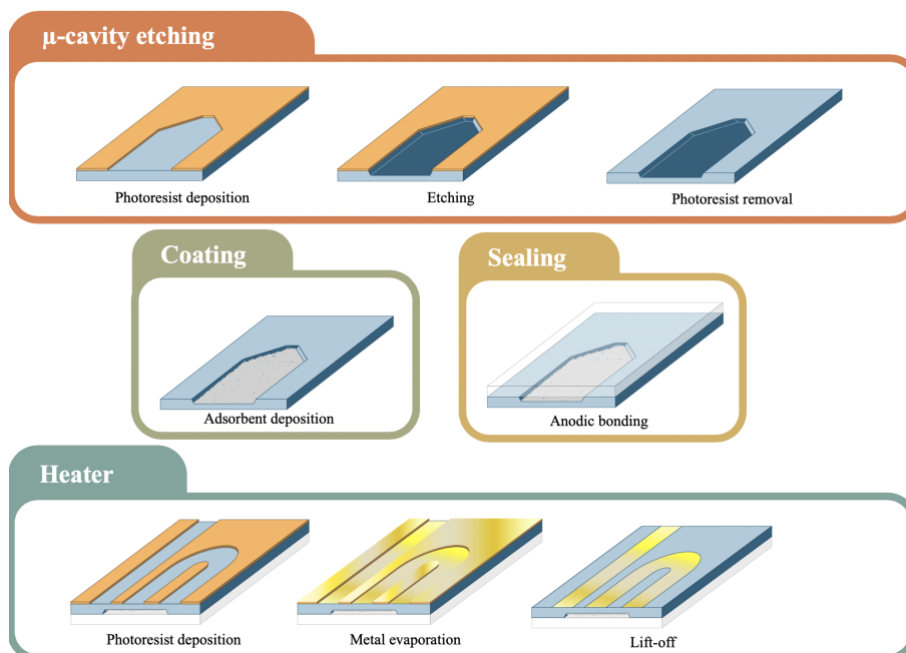
Figure S1. Schematic of microdevice fabrication run.

4' diameter, P doped Si wafers (500 ± 20 µm thickness, <100> crystal orientation, 5 - 10 Ω·cm resistivity) supplied by Sil'Tronix Silicon Technologies were used in all of our devices. For wet etching, a specific negative-working photoresist ProTEK® (Brewer Science) was used. It features a non-degradable character under alkaline etching conditions – which is essential for wet etching. The optical masks were designed using Clewin5® software and printed on high grade acetate film by Micro Lithography Services LTD. The standard optical lithography process is depicted in Figure S2.
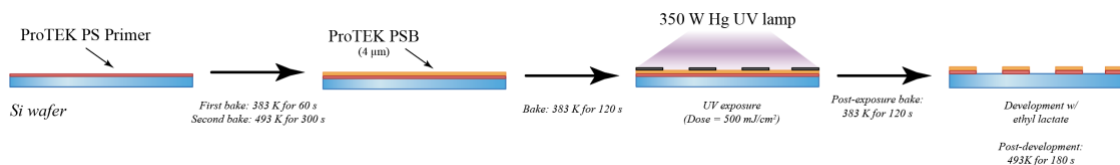
Figure S2. Standard optical lithography process on Si wafer for cavity definition.

Once the photoresist is deposited, the Si wafer is placed in a custom PEEK holder and immersed vertically in a KOH (40%v) bath at 353 K for a set amount of time. Commonly, etching times of 20 min are used for etching depths of 20 µm.
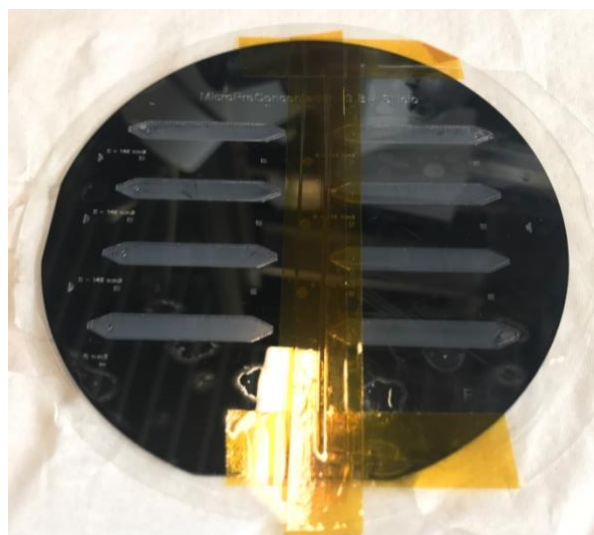

Figure S3. Optical image of the whole 4' diameter Si wafer ready for dicing and anodic bonding.

For the fabrication of Cu-BTC based micropreconcentrators, the coating "step" for adsorbent deposition required the presence of a metallic thin film. This metallic thin film was not performed on the Si cavity but on the top Borofloat cover by standard lift-off process as squematically described in Figure S4.
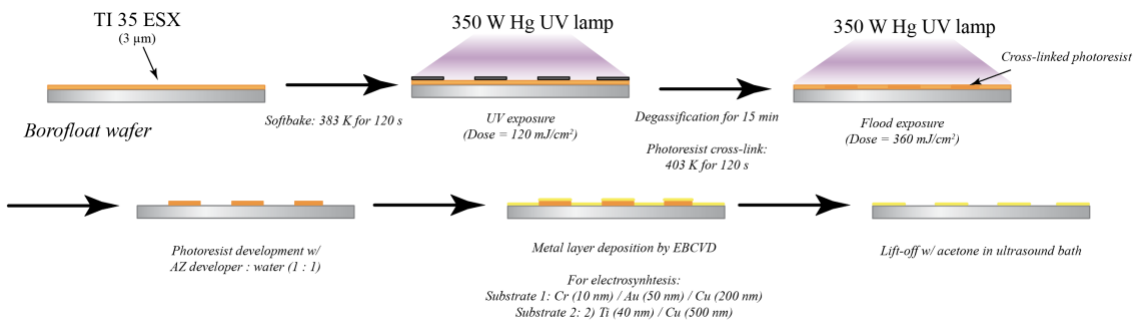
Figure S4. Pattering of metal substrate for electrosynthesis on a Borofloat substrate by standard lift-off process using the photoresist TI35ESX as sacrificial layer.

Section 2. Experimental set-up for the electrochemical synthesis on Cu modified glass substrates
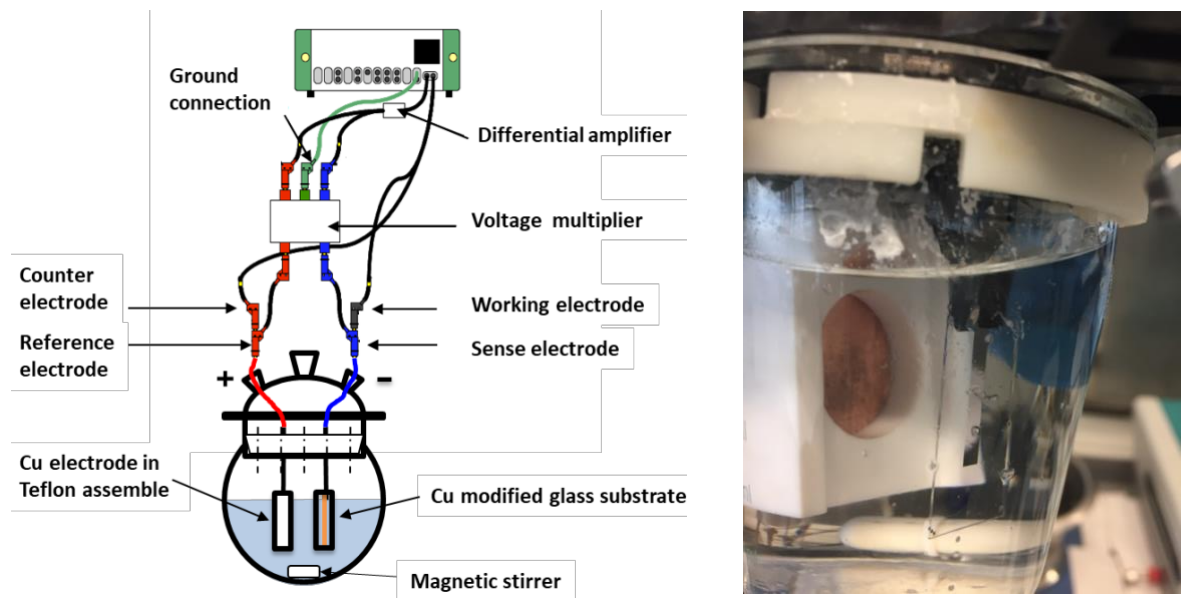
Figure S5. Experimental set-up for the electrochemical synthesis on Cu modified glass substrates: Schematic view of the electrochemical cell (left); optical image of the Cu modified glass working electrode and counter-electrode assembled on a teflon plate (right).

Section 3. Breakthrough Testing of functional micropreconcentrators

Sorption dynamics of the functional μ-preconcentrators were evaluated by analysis of the monitored breakthrough curve. A typical breakthrough curve, as depicted on Figure S6, follows the evolution in time or volume (of circulated gas) of the eluted analyte concentration downstream of the sorption unit. Mostly, the eluted concentration C_x is normalized by the feeding concentration C_0, so it ranges from 0 to 1.
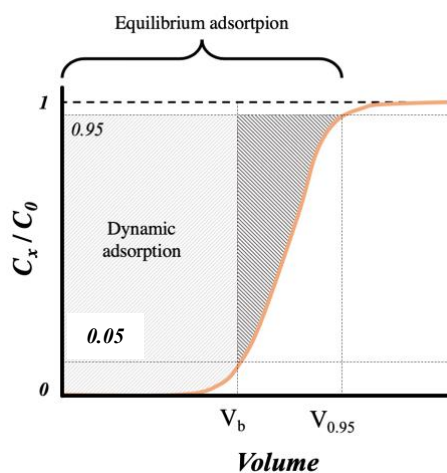
Figure S6. Typical breakthrough curve where the normalized concentration is plotted as a function of the volume that has been circulated inside the sorption unit.

For this work, breakthrough point is considered as the moment where $C_x/C_0 = 0.05$, which implies that the adsorbent is becoming saturated and begins to be unable to trap all the analyte molecules carried by the feeding gas. The moment at which breakthrough takes place is denoted as breakthrough time (t_b). Similarly, the volume that has been fed to the bed is defined as breakthrough volume ($V_b = t_b * Q_{feed}$, being Q_{feed}: feed volumetric flow). The ratio of uptake sorbate (target analyte) mass up to breakthrough point (m_b) to the sorbent mass is defined as dynamic sorption capacity (W_d). Analogously, the point where the adsorbent is exhausted is denoted as saturation point; and in this work is assumed it takes places when $C_x/C_0 = 0.95$, this point determines the equilibrium sorption capacity when working in dynamic conditions (W_e). The

maximum mass of sorbate can be calculated by integrated the area above of the breakthrough curve (up to $C_x/C_0 = 0.95$).
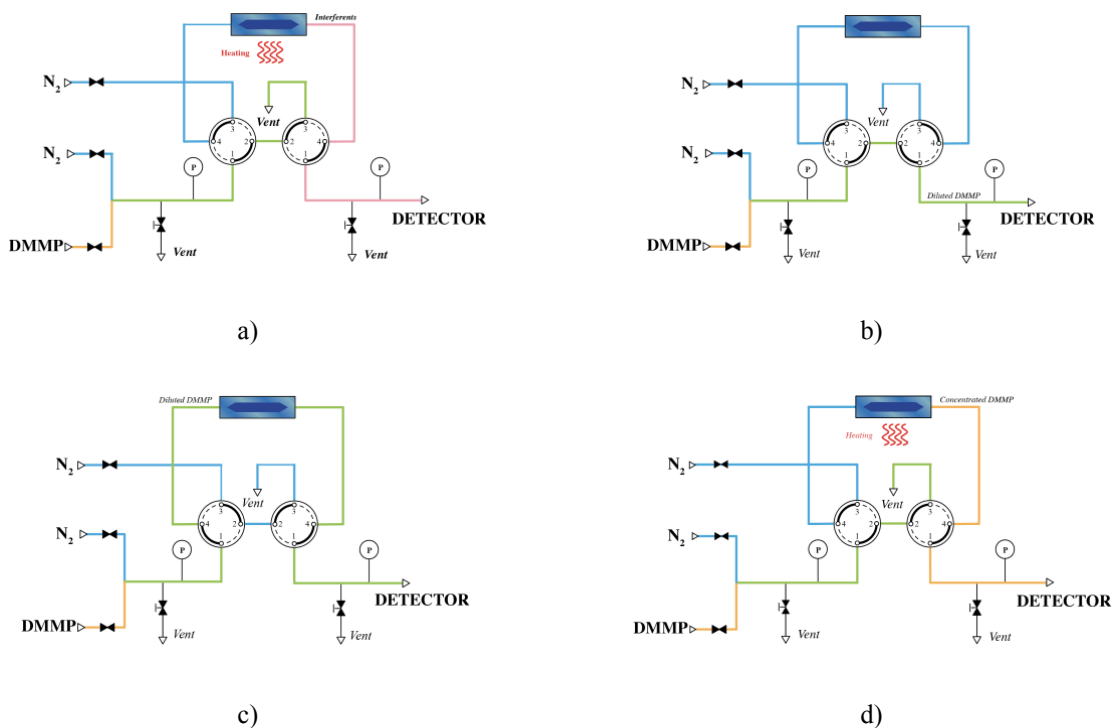

Figure S7. Scheme of flow arrangement in the experimental set-up for breakthrough testing: a) adsorbent pre-treatment, b) analyte baseline, c) analyte adsorption and d) analyte desorption.

A conventional breakthrough test comprises the following steps (see Figure S7) depicts the schematics of the set up installed at the University of Zaragoza):

1. *Adsorbent pre-treatment*: before the adsorption experiment, the adsorbent is regenerated thermally by placing the microdevice on a hotplate at 200 ºC while inert N_2 sweeps the cavity and degas the sorptive layer. Ideally this step is performed until no undesirable specie was detected.

2. *Analyte baseline*: analyte was fed directly into the detector to obtain the baseline signal that is used for calibration. To avoid contamination on the adsorbent material, dry N_2 is circulated through the microdevice while this step takes place.

3. *Analyte adsorption:* analyte is fed to the microdevice until sorbent saturation, which is assessed by previous calibration ($C_{exit} = C_0$).

4. *Analyte desorption:* the analyte was desorbed under the same conditions as step 1.

Section 4. Experimental Set-up for Preconcentration Factor Determination

Preconcentration experiments were performed with atmospheres of 2.65 mg/m^3 (520 ppbV) of DMMP in dry N$_2$. Although this concentration is 8-fold higher than reported lethal value for sarin gas for exposure times up to 10 min (AEGL-3 = 0.38 mg/m^3, 64 ppbV), it is fairly reasonable value to accurately characterize the μ-device performance at a reproducible concentration without the need to use additionally dilution streams. The synthetic DMMP/N$_2$ mixture was generated by circulating 10 STP cm^3/min of dry N$_2$ through a calibrated permeation tube of DMMP (VALCO, permeation rate of 148.41 ng/min ± 3.07 at 90 ºC) and fed to the μ-device. The monitoring of the desorption peak was performed with a gas chromatograph coupled with a mass spectrometry detector (GCMS, Shimadzu GCMS QP2010) downstream the μ-device. The characteristic DMMP mass signals were followed (m/z = 79, 94, 109, 124) as well as the principal uma signals of the main decomposition products: methanol (m/z = 31), dimethyl ether (m/z = 45), CO$_2$ (m/z = 44) and formaldehyde (m/z = 29).

The μ-device is connected to the GCMS 6-port valve through capillary tubing (320 μm inner diameter) though high temperature septum glued to the Borofloat side of the device. In order to avoid adsorption of the DMMP in the faces of the septa, an intermediate layer of Kapton has been placed between the Borofloat side and the septum. This approach relies on the rapid thermal desorption of DMMP and the adequate carrier flow rate to push out the bolus in a plug-flow fashion, without the need of a focusing stage. Thus, the experimental protocol is reduced to the sampling of DMMP at room temperature and 10 cm^3/min for certain time, the flushing out of the DMMP molecules in gas phase with GCMS carrier for 5 min, after which, the adsorbent is rapidly heated at 523 K, releasing the DMMP and being pushed out to the detector by the GCMS carrier (see Figure S8).
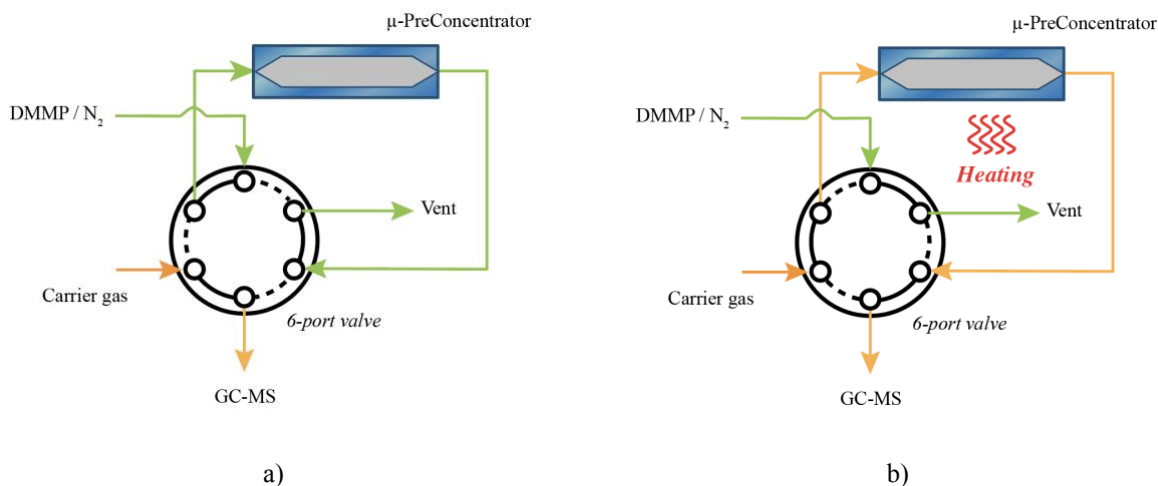
Figure S8. Dynamic preconcentration set-up. a) sampling of the DMMP/N₂ mixture. b) Thermal desorption and concentration of the DMMP adsorbed. Between a) and b) takes place a flushing stage (not depicted in the figure). Green line depicts DMMP/N₂ flow path whereas orange line depicts He flow path.

The preconcentration performance of the μ-device as sampling unit is evaluated from its preconcentration coefficient, denoted as K. According to IUPAC guidelines, this value is defined as the ratio of the gas sample collected volume to the volume in which that same mass is released according to the quantification at the point of detection, assuming no transfer mass losses take place. Accordingly, the *K* estimation is carried out under experimental conditions that guarantee the absence of target molecules in the outlet stream, *i.e.* no breakthrough conditions. Thus, given a desorption peak (see Figure S9), the preconcentration coefficient *K* is calculated as follows:

$$K = \frac{V_{sample\ collected}}{V_{sample\ desorbed}} = \frac{Q_{sampling} * t_{sampling}}{Q_{desorption} * FWHM}$$

where $Q_{sampling}$ is the feeding flow rate, $t_{sampling}$ is the sampling time, $Q_{desorption}$ is the flow rate at which the released sample is being flushing out and FWHM is the full width at half maximum of the desorption peak registered by the detector.
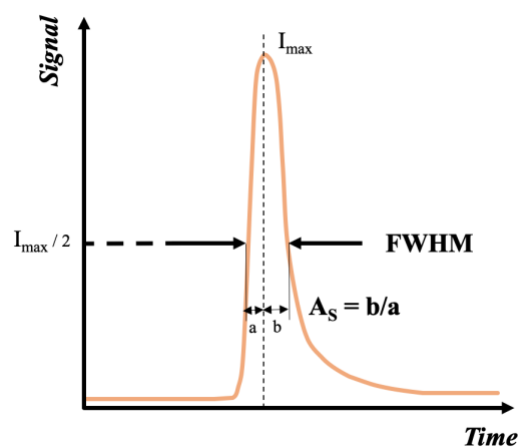
Figure S9. Graphical representation of a typical desorption peak. On the graph are shown the most important descriptive parameters: peak height I_{max}, full width at half maximum (FWHM) and the asymetric factor A_S.

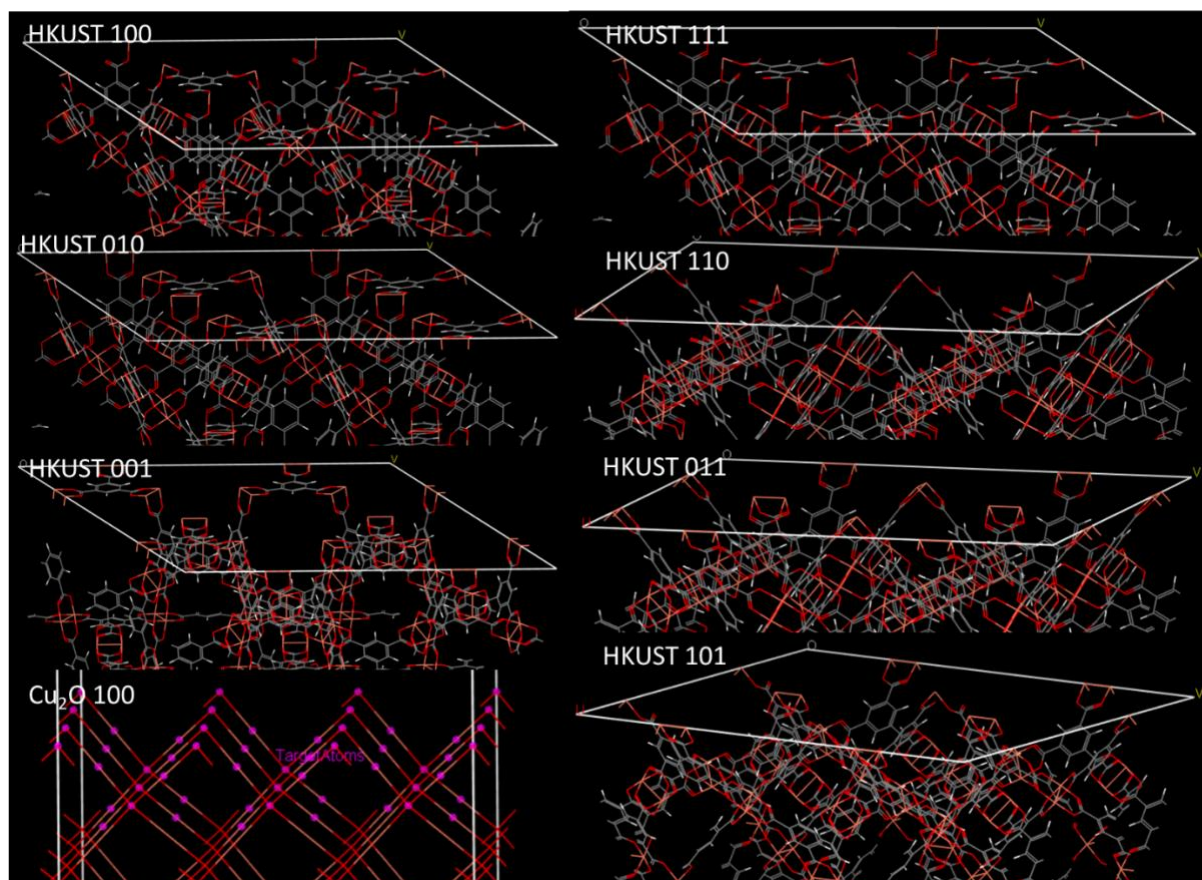**Section 5.** Morphologies of the structures used for Montecarlo Simulations

Figure S10. Atomistic representation of Cu₂O and Cu-BTC (HKUST) vacuum slabs with different surface orientations.

HKUST (100) = (111)

HKUST (010) = (0011)

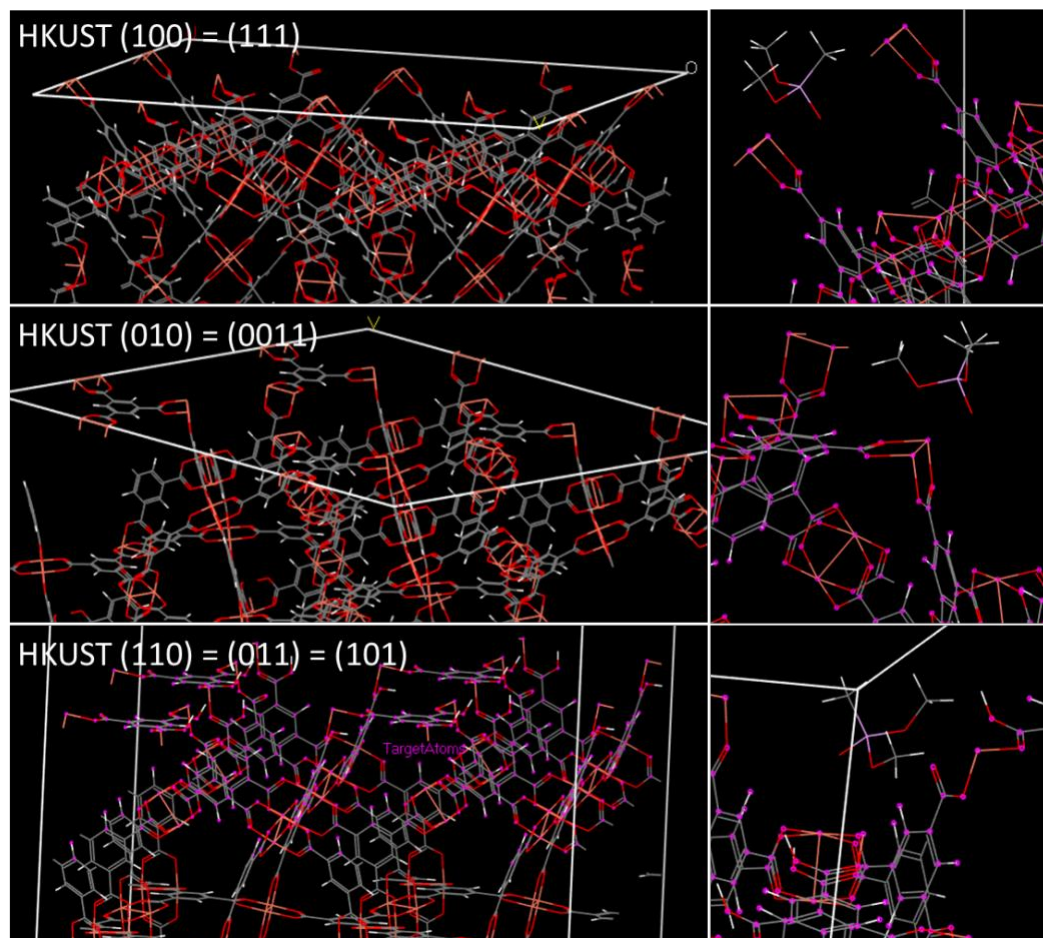HKUST (110) = (011) = (101)

TargetAtoms

Figure S11. Atomistic representation of the energy minimized structures for adsorption of DMMP molecules over Cu-BTC (HKUST) vacuum slabs at different crystal orientations.
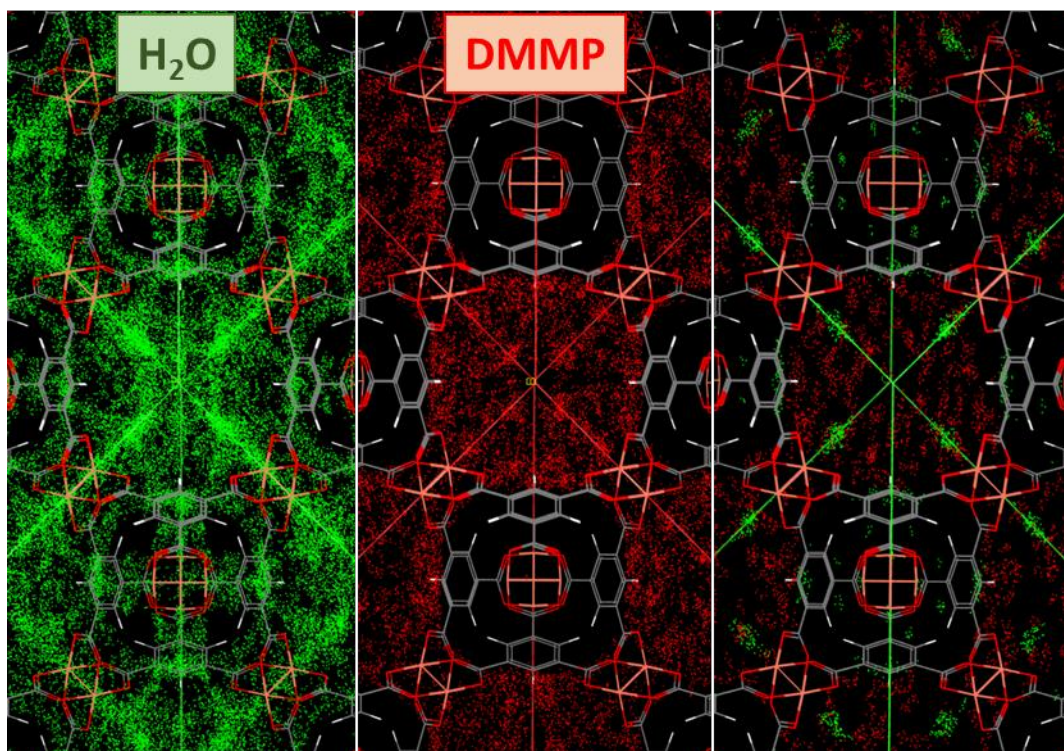
Figure S12. Adsorption Sites for water (green color) and DMMP (red color) molecules onto Cu-BTC structure.

Section 6. Durability and Stability of Cu-BTC functional microdevices

The durability and stability of the Cu-BTC functionalized μ-devices were confirmed by assessment of the sorption properties upon exposure to several sorption-desorption cycles of DMMP. The breakthrough curves obtained with a #4_15 type functional device, along 1 month testing and being uninterruptedly exposed to ambient air, are shown below. The data analyses reveal an average value of 67.6 ± 1.5 mg/g and 664.4 ± 47.0 mg/g for dynamic and equilibrium adsorption capacities, respectively. These results confirm the stability of the Cu-BTC sorption capacity, and the reusability of the functional microdevices.
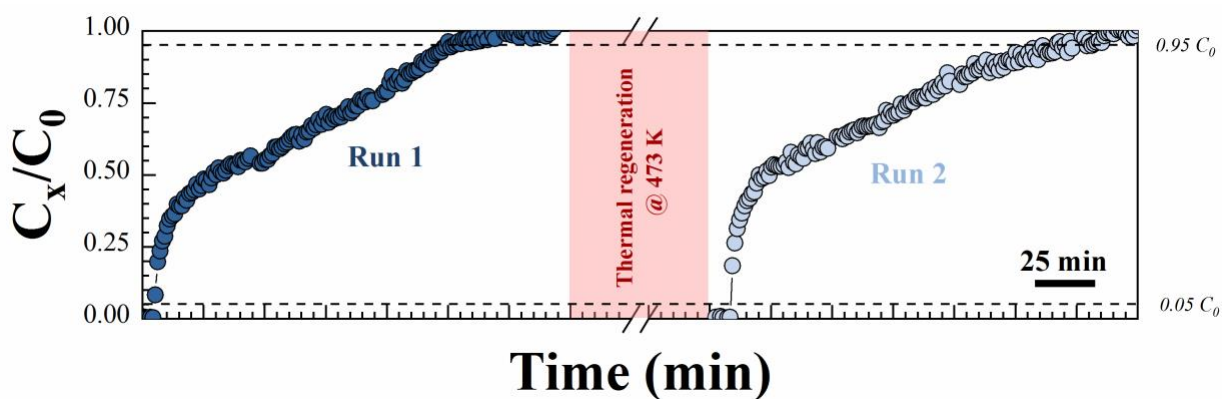

Figure S13. Performance of functional Cu-BTC μ-preconcentrator exposed to sequential adsorption-desorption cycle. Run 1 corresponds to the first breakthrough curve. Run 2 shows the breakthrough curve after 1 month testing, i.e. above 20 sorption/desorption cycles. Experimental conditions: Adsorption 162 mg/m³ (32 ppmV) of DMMP 10 STP cm³ /min dry N₂; Desorption 12 h at 473 K 10 STP cm³ /min dry N₂.